ACS Catalysis

pubs.acs.org/acscatalysis Research Article

Mechanistic and Structural Insights into the Liquid-Phase Oxidation of Cyclohexane over $LaCo_{0.7}Fe_{0.3}O_3$ Perovskite Nanoparticles

Akhil Hareendran, Takuma Sato, Maik Dreyer, Anna Rabe, Soma Salamon, Niklas Sülzner, Ulrich Hagemann, Catalina Leiva-Leroy, Nicolas Cosanne, Krishnan Ravi, Dongsheng Zhang, G. Wilma Busser, Malte Behrens, Christof Hättig, Heiko Wende, Alexander Schnegg,* and Martin Muhler*

Cite This: *ACS Catal.* 2025, 15, 12773−12789 Read Online

ACCESS | Metrics & More | Article Recommendations | Supporting Information

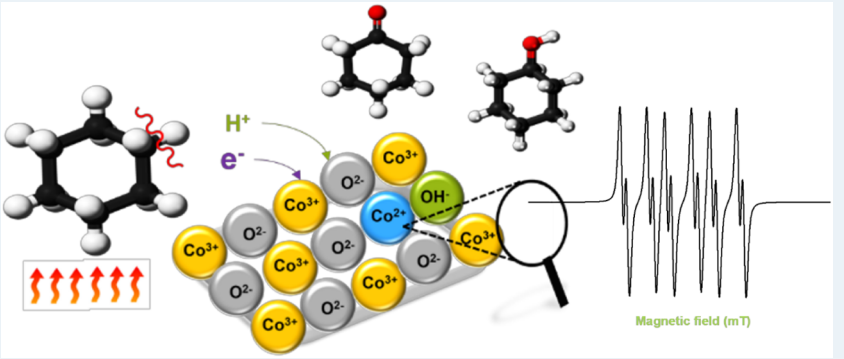

ABSTRACT: The aerobic liquid-phaa$Co_{0.7}Fe_{0.3}O_3$ perovskite under mild conditions exhibited an enhanced selectivity toward KA oil (mixture of cyclohexanol and cyclohexanone) at high conversion. Mechanistic investigations revealed a partial reduction of Co^{3+} to Co^{2+} in the surface region during the activation of the C−H bond. The selectivity differences induced by adding the catalyst were qualitatively analyzed using *in situ* ATR-IR spectroscopy. The radical scavenging studies and spin trap EPR confirmed the crucial role of cyclohexylperoxyl ($C_6H_{11}OO^{\bullet}$), cyclohexyloxyl ($C_6H_{11}O^{\bullet}$), hydroxyl ($HO^{\bullet}$) and cyclohexyl ($C_6H_{11}^{\bullet}$) radicals in the reaction. Scavenging $C_6H_{11}OO^{\bullet}$ during the uncatalyzed reaction strongly increased the stability of KA oil. Postreaction characterization by XRD, XPS, TPR, Mössbauer, magnetometry, EPR, and Raman spectroscopy confirmed the partial reduction of Co^{3+} and the formation of an additional Co-rich LDH phase during cyclohexane oxidation. DFT calculations of the cyclohexyl hydroperoxide (CHHP) decomposition pathways provided evidence that α-H abstraction is highly favored (33 kJ/mol) compared with the homolytic O−O cleavage (127 kJ/mol) in the absence of a catalyst and validated the influence of the catalyst on the homolytic O−O cleavage of CHHP via the Haber-Weiss reaction. A catalytic cycle based on mixed oxyhydroxy Co dimers is proposed to rationalize the influence of the catalyst in controlling highly oxidizing $C_6H_{11}OO^{\bullet}$ radicals, thus favoring KA oil stability.

KEYWORDS: *cyclohexane oxidation, in situ ATR-IR spectroscopy, radical scavenging, computational chemistry, EPR spectroscopy, spin trap EPR, XPS, Mössbauer spectroscopy*

1. INTRODUCTION

Owing to their versatile properties, perovskite-type materials possess numerous applications in the fields of energy storage, fuel cells, catalysis, or sensors.[1−6] About 90% of the metallic elements crystallize in the perovskite structure with isotropic, anisotropic and amorphous morphologies.[7,8] In general, perovskites are represented as ABO_3, where A represents a relatively larger cation than the B cation usually belonging to the lanthanides, alkaline, or alkalineearth metals. The partial substitution of these metal cations ($A_{1x}A'_xB_{1x}B'_xO_3$) provides various possibilities to induce different materials properties for specific applications.[9−12] Especially, the 3d metal-substituted perovskites have been widely used as heterogeneous catalysts in several hydrocarbon oxidation reactions.[13,14]

Aerobic oxidation of hydrocarbons is one of the vital industrial processes as it is used to produce specialty chemicals. Hydrocarbon combustion is an example of a total oxidation

Received: April 29, 2025
Revised: June 25, 2025
Accepted: July 1, 2025
Published: July 14, 2025

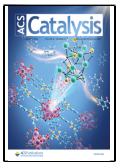

https://doi.org/10.1021/acscatal.5c02919
ACS Catal. 2025, 15, 12773−12789

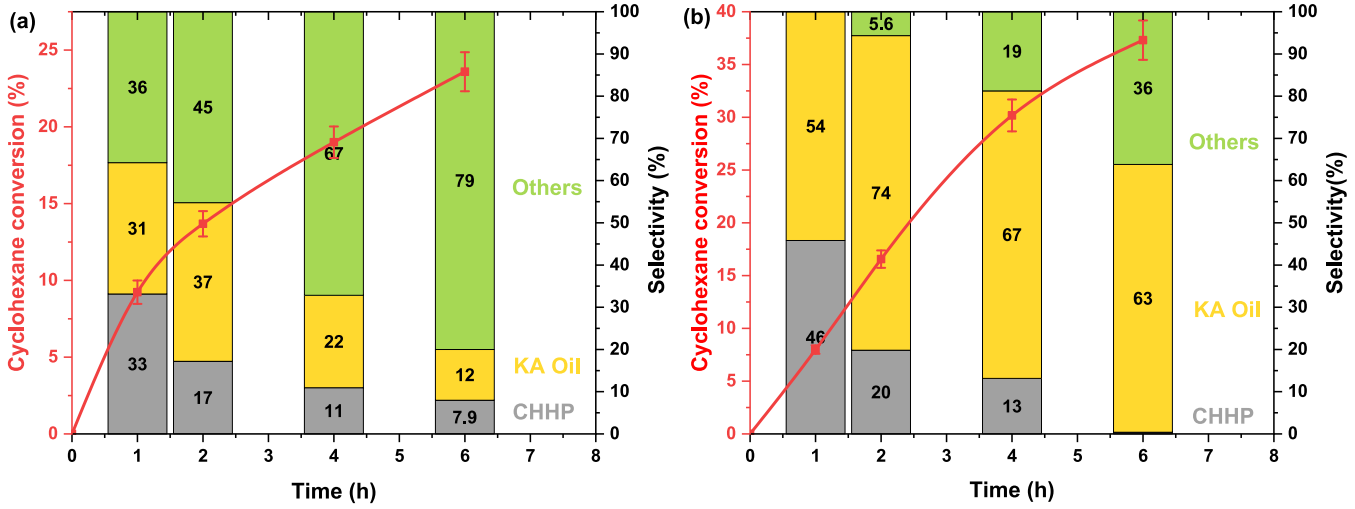

Figure 1. Conversion-selectivity profiles of the (a) uncatalyzed reaction and (b) catalyzed reaction using 20 mg $LaCo_{0.7}Fe_{0.3}O_3$. Reaction conditions: 130 °C, 1.00 mol/L cyclohexane, 15 bar O_2, 600 rpm, 6 h, acetonitrile as solvent, and biphenyl as internal standard.

reaction, where CO_2 and H_2O are produced as the final products and heat is released.[15] Additionally, the selective oxidation of hydrocarbons generates commercially valuable chemicals such as terephthalic acid (TPA),[16] ethylene oxide,[17] or acrylic acid.[18] Especially, the liquid-phase oxidation of cyclohexane is of great importance, because the formed mixture of cyclohexanol and cyclohexanone (KA oil) is used as a precursor for the synthesis of Nylon-6.[19−22] The higher reactivity of KA oil limits its selectivity, particularly at high conversion.[23] Several homogeneous catalysts have already been reported to maintain high selectivity with increasing conversion.[24−26] However, the challenges in separation and reusability limit its potential in upscaling and led to the development of novel heterogeneous catalysts.[27−31] La-based perovskites have been thoroughly investigated for the liquid-phase oxidation of both cyclohexane and cyclohexene using oxidizing agents such as molecular oxygen, hydrogen peroxide or *tert*-butylhydroperoxide ($(CH_3)_3COOH$, TBHP).[14,32−35] Various catalysts with different transition metal compositions have already been reported,[13,21,32,33] while further research is essential to enhance effectiveness and to develop more suitable catalysts for sustainable cyclohexane oxidation. With multifunctional catalysts, hazardous oxidizing agents such as HNO_3, H_2O_2, and TBHP could be excluded from use. La-based catalysts appear to be promising in defect engineering providing oxygen vacancies that enable an effective oxidation using molecular oxygen.[36−40] It is known that free radicals formed by C−H bond breaking (initiation) are the active species for promoting the reaction to the desired products in cyclohexane oxidation.[23,29] However, establishing reliable correlations between the catalytically relevant surface properties and free radical activity remains challenging. Tracking the type and population of free radicals over reaction time along with the catalytic activity could be a step forward revealing the essentials to favor selective pathways in autocatalytic oxidation reactions.

Previously, a series of $LaCo_xFe_{1-x}O_3$ catalysts synthesized via coprecipitation was screened and found to be active in the aerobic liquid-phase oxidation of cyclohexane under mild reaction conditions.[41,42] A high conversion of 14.8% was achieved with 95% KA oil selectivity for $LaCo_{0.7}Fe_{0.3}O_3$ at a temperature of 120 °C. In this work, we investigate the catalytic cyclohexane oxidation over $LaCo_{0.7}Fe_{0.3}O_3$ perovskite nanoparticles in the liquid phase applying a mechanistic approach, in which insights into the properties and influence of the free radicals in the desired product formation (KA oil) and the role of the catalyst are provided by monitoring the formation and conversion of these free radicals. Several postreaction characterization techniques such as X-ray diffraction (XRD), X-ray photoelectron spectroscopy (XPS), H_2 temperature-programmed reduction (TPR), Raman spectroscopy, and electron-paramagnetic resonance (EPR) spectroscopy were employed to study this correlation and support the reaction mechanism hypothesized earlier.[41]

2. RESULTS AND DISCUSSION

2.1. Catalyst Synthesis and Characterization. The $LaCo_xFe_{1-x}O_3$ perovskites were synthesized via coprecipitation.[41,42] using a mixture of NaOH and Na_2CO_3 at a constant pH of 9.5. To study the effect of Co substitution, x had been varied in the range from 0.00 to 0.70 in our previous study.[42] The increments from $x \geq 0.4$ resulted in undesirable phase segregation but with a very low phase fraction (<5% Co_3O_4). To confirm the phases formed, preliminary characterization had been performed using X-ray diffraction (XRD) and transmission electron microscopy (TEM). Figure S1 shows the X-ray diffraction patterns for the catalyst series from our previous study. An orthorhombic phase was only identified for the materials with $x < 0.4$ and was referenced with ICSD code 6296 ($LaFeO_3$). As the degree of Co substitution in the $LaFeO_3$ lattice increased, a gradual shift in the (112) reflection confirmed the Co^{3+} incorporation in agreement with previous reports.[43,44] Besides the $LaFeO_3$-like orthorhombic phase, two distinct additional phases, a $LaCoO_3$-like rhombohedral (ICSD-33969) and a Co_3O_4-like spinel (ICSD-9362) phase, were also found in the diffractogram. To further analyze the lattice parameters and phase composition, Rietveld refinement was carried out and summarized in Table S1. N_2 physisorption measurements determined the specific surface areas of the nanoparticles within 7-30 m^2/g and particle sizes of 20-23 nm.

2.2. Cyclohexane Oxidation and In Situ ATR-IR Spectroscopy. The reported $LaCo_xFe_{1-x}O_3$ perovskite series had been screened for aerobic liquid-phase oxidation of cyclohexane in our previous work.[41] Uncatalyzed experiments

https://doi.org/10.1021/acscatal.5c02919
ACS Catal. 2025, 15, 12773−12789

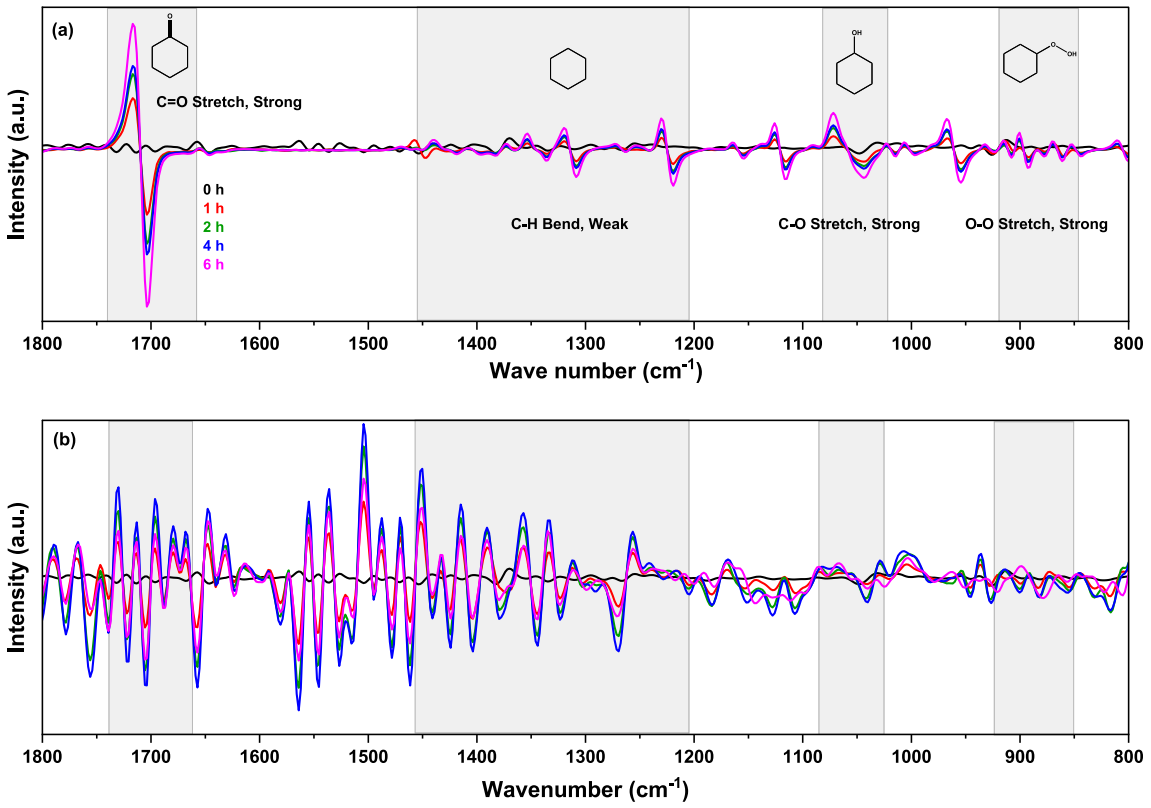

Figure 2. First derivative of the *in situ* ATR-IR spectra of (a) catalyzed and (b) uncatalyzed reactions (0 h (black), 1 h (red), 2 h (green), 4 h (blue), 6 h (pink) in the range of 1800−800 cm^{-1} after background subtraction. Reaction conditions: 130 °C, 1.00 mol/L cyclohexane, 20 mg $LaCo_{0.7}Fe_{0.3}O_3$, 15 bar O_2, 600 rpm, 6 h.

performed at 120 °C and 1.00 mol/L cyclohexane in acetonitrile resulted in a conversion of 3.3% after 6 h. The reaction was also associated with an induction period of 2 h as shown in Figure S2. The observed induction period was in agreement with similar studies on hydrocarbon oxidation, where initial, but short time intervals were reported to facilitate the free radical generation in the absence of a catalyst.[45−48] To optimize the reaction parameters with a minimal influence of temperature on product selectivity, a relatively low temperature of 120 °C was initially set. For screening the catalysts, 120 °C, 15 bar O_2, 1.00 mol/L cyclohexane, 600 rpm, and 6 h were chosen as reaction conditions. Figure S3 shows the overall conversion-yield profile for the catalysts screened for cyclohexane oxidation. Around 4% conversion was observed for $LaFeO_3$ similar to the uncatalyzed reaction suggesting catalytic inactivity. The influence of Co substitution into the $LaFeO_3$ lattice was evident with the improved catalytic activity even at a lower substitution of $x = 0.05$ (phase-pure, Table S1). Higher Co substitution (%) improved the catalytic performance with a higher degree of conversion (≈ 15% for $x = 0.7$) and higher KA oil selectivity (95%). The improved activity due to Co-substitution is attributed to its role in decomposing cyclohexylhydroperoxide (CHHP). The existence of a free radical mechanism and the presence of cyclohexyloxyl and cyclohexylperoxyl radicals were confirmed using EPR spectroscopy.[41]

With the introduction of the catalyst ($x = 0.7$), it was possible to lower the reaction temperature to 110 °C. In addition, immediate catalytic conversion without induction phase was observed (Figures S2 and S4). While the uncatalyzed reaction had an activation energy of 170.4 kJ/mol (Figure S3a),[41] the activation energy of the catalyzed reaction was lower by 43 kJ/mol following first-order kinetics (Figure S4), and by using EPR spectroscopy, the type and the temporal change of the radicals over the reaction course were identified.

Figure 1 shows a comparison between the conversion-selectivity profiles for the uncatalyzed and the catalyzed reaction. To conduct systematic spin trap experiments and to precisely identify the individual radicals present, optimal and comparable reaction conditions with considerable performance both in the presence and absence of the catalyst had to be chosen. Therefore, reactions were performed at 130 °C, 15 bar O_2, 1.00 mol/L cyclohexane in acetonitrile, 600 rpm and 6 h.

A conversion of 23.6% was achieved after 6 h with a KA oil selectivity of 12% for the uncatalyzed reaction (Figure 1a). During the initial hour 33% selectivity to CHHP and 31% to KA oil were found, while similar amounts of byproducts were also identified with about 36% selectivity. The identified byproducts were cyclohexane-1,2-diol, cyclohexane-1,2-dione, cyclohexane-1,4-dione, 2-hydroxycyclohexanone, and 7-oxabicylo[4.1.0]heptan-2-one. In addition, this time period represents the early phase of an autocatalytic reaction, where the formed CHHP intermediate is primarily decomposed to KA oil and further oxidized to byproducts. This observation confirms that the formed KA oil is not stable under the reaction conditions and undergoes overoxidation as soon as it is formed. In addition to KA oil formation, the initial hours are a favorable period of time for the generation of radicals which further take part in the oxidation during the subsequent hours. Therefore, KA oil may only be relatively stable during the first hour in uncatalyzed reactions owing to the relatively lower

https://doi.org/10.1021/acscatal.5c02919
ACS Catal. 2025, 15, 12773−12789

amount of radicals available for its overoxidation. CHHP and KA oil decompose subsequently, and a following increase in byproducts is observed. Thus, an autocatalytic reaction in cyclohexane oxidation is observed where the primary products are consumed to form further products.[47,49,50]

Figure 1b shows the reaction profile upon the addition of $LaCo_{0.7}Fe_{0.3}O_3$ as catalyst. KA oil was the major product still after 6 h at a relatively higher degree of conversion of 37.3% and selectivity of 63%. The selectivity profile confirms the stability of KA oil over the course of reaction. In addition, CHHP decomposition was also relatively efficient with complete decomposition at the sixth hour. Nevertheless, byproduct formation seems to be unavoidable, as a notable amount is formed from the fourth hour onward. To compare the two reactions based on KA oil selectivity, similar degrees of conversion should be considered. At X = 16.7% for the catalyzed reaction, the KA oil selectivity amounts to 74%, and at X = 18.3% for the uncatalyzed reaction, KA oil selectivity equals 22%. Therefore, the added catalyst is highly favoring KA oil selectivity. Even though the maximum achieved KA oil selectivity of 74% is decreasing gradually after X = 16.7%, it still remains the major product over the reaction course. The reaction in general is autocatalytic in nature, and a 100% KA oil selectivity cannot be kept up to X = 100%. In the presence of the catalyst a higher degree of conversion is achieved where KA oil is still stable and a major product of cyclohexane oxidation. Consequently, this study further attempts to understand the stability increase for KA oil in the presence of $LaCo_{0.7}Fe_{0.3}O_3$ as catalyst.

To visualize the product distribution qualitatively, *in situ* ATR-IR (attenuated total reflection infrared) spectroscopy was carried out. Figure 2 shows the first derivative of the ATR-IR spectra obtained during the catalyzed and uncatalyzed reactions. Initially, the calibrations were performed using standard solutions prepared in acetonitrile, and the characteristic bands were recorded as shown in Figure S5. We were unable to record or identify the characteristic CHHP vibrations due to the difficulty in synthesizing it at room temperature conditions.

For approximate identification of the hydroperoxyl vibrations, a comparable reference (2-cyclohexene-1-hydroperoxide) from our previous studies on cyclohexene oxidation was used.[51] Since the measurements aimed at verifying the product differences of stable products in catalyzed and uncatalyzed reactions, CHHP identification was not considered crucial. For real-time measurements, the reaction mixture was monitored constantly every 2 min. The reaction was initiated by flushing O_2 to the heated batch reactor equipped with the ATR-IR probe and containing the reaction mixture. An initial spectrum was recorded and used as background (0 h in Figure 2) in the further measurements.

Generally, the IR spectrum of cyclohexane is dominated by two strong vibrations, one around 2900 cm^{-1} (most intense; sp^3 C−H stretching) and one around 1500 cm^{-1} (second intense; C−H bending).[52,53] Within our calibration step (Figure S5), we observed that only the dominant C−H stretching vibrations were detected in the group-frequency region (4000−1800 cm^{-1}). To visualize the product differences, Figure 2 exclusively exhibits the fingerprint region (≈1800−800 cm^1), and therefore only weak C−H bending modes are visible for cyclohexane. The figure only intends to validate the selectivity differences as shown in Figure 1. Figure 2a depicts the catalyzed reaction where the strong band of the carbonyl (C=O) stretching vibration of cyclohexanone is observed around 1710 cm^{-1}. Its intensity increased over reaction time reflecting the increasing concentration in the reaction mixture. The C−O stretching vibration at 1070 cm^{-1} is assigned to cyclohexanol. A relatively lower intensity was also observed for this band during calibration (Figure S5) when compared to the C=O stretching band. The stronger O−H stretching vibration occurs around 3400 cm^{-1} and falls in the group-frequency region. Figure 2b shows the IR spectrum of the uncatalyzed reaction where both C−O and C=O stretching vibrations were either completely or partially diminished compared with Figure 2a due to the further oxidation of the KA oil to byproducts as shown in Figure 1. For example, the single stretching vibration (C=O) at 1710 cm^{-1} is split into several distinct peaks with lower intensities pointing to the further oxidation of cyclohexanone to cyclohexane-1,2-dione, cyclohexane-1,4-dione, or 2-hydroxycyclohexanone. The gradual increase of the bands between 1600 and 1200 cm^{-1} suggests a temporal increase in the cyclic products (C−H, C−C weak bending; byproducts) in the uncatalyzed reactions.

2.3. Radical Scavenging Experiments. Radical scavenging experiments were performed to identify the type of free radicals present. TEMPO ((2,2,6,6-tetramethylpiperidin-1-yl)oxyl) is a widely used spin-trap agent in EPR spectroscopy, but can also be used as a broad-spectrum scavenger in free-radical reactions.[52,53] *p*-Benzoquinone (PBQ) belongs to the quinone family of compounds that are used mainly to scavenge superoxyl and peroxyl radicals.[54,55] *tert*-Butanol (TBOL) reacts with radicals containing single oxygen atoms such as hydroxyl or alkoxyl radicals.[56,57]

Figure 3 shows the conversion profiles during the radical scavenging experiments without catalyst. Data points in green

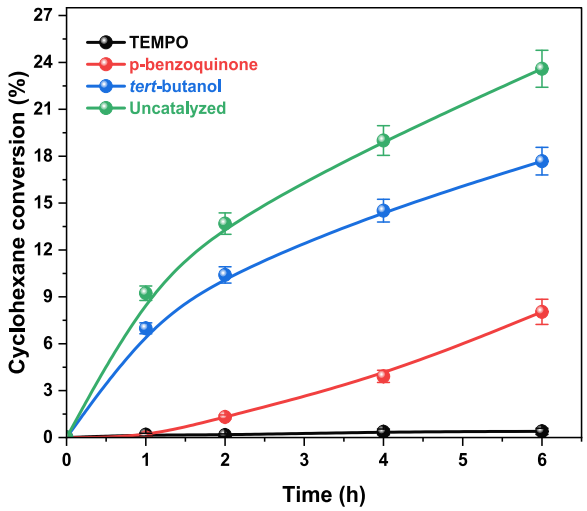

Figure 3. Conversion-reaction time profiles of the radical scavenging experiments in the uncatalyzed reaction. Reaction conditions: 130 °C, 1.00 mol/L cyclohexane, 15 bar O_2, 600 rpm, 6 h, 2 mol % of radical scavenger, acetonitrile as solvent, and biphenyl as the internal standard.

refer to the uncatalyzed reaction and are used as a basis for comparison. First, TEMPO was introduced as the broad-spectrum scavenger (data points in black) to validate the existence of free-radicals in general. As expected, the reaction was quenched resulting in the absence of any observable

https://doi.org/10.1021/acscatal.5c02919
ACS Catal. 2025, 15, 12773−12789

degree of conversion even after 6 h demonstrating that free radicals are the active species that propagate cyclohexane oxidation under the applied conditions.

Upon addition of PBQ during the uncatalyzed reaction, the degree of conversion significantly decreased from 23.6% (UC) to 8% after 6 h. Therefore, it is likely that cyclohexylperoxyl radicals ($C_6H_{11}OO^\bullet$) are crucial in the reaction facilitating the formation of the CHHP intermediate by hydrogen abstraction from cyclohexane. Despite a decrease in conversion to 17.7% upon TBOL addition, the overall temporal change in conversion seems to be less significant compared with the reaction involving PBQ. Based on these experiments, it has to be assumed that the uncatalyzed reaction involves cyclohexylperoxyl ($C_6H_{11}OO^\bullet$), cyclohexyloxyl ($C_6H_{11}O^\bullet$), hydroxyl ($HO^\bullet$) and cyclohexyl ($C_6H_{11}^\bullet$) radicals. These results are in good agreement with our previous EPR observations (Figure S6), where the spectral simulations of the EPR spectra revealed the presence of these species.[41] For comparison, the conversion-selectivity profiles of these studies are shown in Figures S7 and S8. Scavenging studies based on catalyzed reactions were also performed for further comparison. As selectivity comparisons of reactions with different degrees of conversion are rather vague, product selectivities at similar degrees of conversion are summarized in Tables S2 and S3.

Figure S7 shows scavenging studies with PBQ aimed at $C_6H_{11}OO^\bullet$ (S7a shows reaction without catalyst and PBQ; S7b shows reaction with catalyst and PBQ; S7c shows the selectivity comparison at the sixth hour). To compare the selectivity (Table S2), a similar range of conversion between 8 and 9% was considered. For the uncatalyzed reaction without PBQ (X = 9.2%; first h), a KA oil selectivity of 31% was obtained with 36% byproducts. The CHHP intermediate remained at a selectivity of 33%. Clearly, the KA oil was overoxidized to byproducts during the first hour of reaction. For the uncatalyzed reaction with PBQ (X = 8%; sixth hour), the selectivity to KA oil remained at 74%, while CHHP and byproducts remained at 11% and 15%, respectively. It is likely that the stability of KA oil increases upon scavenging $C_6H_{11}OO^\bullet$ radicals. An initial assumption could be made based on the highly oxidizing nature of $C_6H_{11}OO^\bullet$ radicals that further oxidize KA oil to byproducts. As indicated by Figure 3, the $C_6H_{11}OO^\bullet$ radicals are dominant and crucial in propagating the reaction further. Upon scavenging, these radicals seem to be participating significantly less in the reaction thereby improving the KA oil stability. The decrease in byproduct selectivity from 79% (without scavenging) to 15% (with scavenging) also implies that $C_6H_{11}OO^\bullet$ is the radical facilitating overoxidation. For the scavenging reactions with catalyst, KA oil (S = 54−57%) and CHHP (S = 43−46%) remained as the main products. It seems likely that the selective oxidizing nature of the catalyst is not significantly influenced by scavenging $C_6H_{11}OO^\bullet$, because the catalyst seems to facilitate CHHP decomposition even in the absence of $C_6H_{11}OO^\bullet$. Furthermore, at a similar conversion of 15−16%, the KA oil selectivity improved from 74% (without PBQ, second h) to 88% (with PBQ, sixth h) upon scavenging $C_6H_{11}OO^\bullet$. The combined effects of PBQ and catalyst seem to suppress the detrimental reactivity of $C_6H_{11}OO^\bullet$ resulting in higher KA oil stability. This observation further supports our initial hypothesis on the origin of enhanced KA oil selectivity in catalyzed reactions due to controlling the $C_6H_{11}OO^\bullet$ population.

In addition to $C_6H_{11}OO^\bullet$ scavenging, Figure S8 exhibits the conversion-selectivity profiles for TBOL-added studies aimed at scavenging $C_6H_{11}O^\bullet$. Figure S8a shows the reaction without catalyst and TBOL, Figure S8b shows the reaction with catalyst and TBOL, and Figure S8c shows the selectivity comparison at the sixth hour. No significant differences were observed in the uncatalyzed reactions with and without scavenging. As shown in Table S3, at a similar conversion of 17.7−19%, byproducts were the main components with 67−73% selectivity. This is expected as the highly oxidizing $C_6H_{11}OO^\bullet$ radicals were still present in the reaction system. Even though the selectivity profile (Figure S8c) for catalyzed reactions shows 20% CHHP left undecomposed upon scavenging, this was not observed in comparison for similar degrees of conversion. The detected CHHP after 6 h in Figure S8c may be due to the lower degree of conversion compared with the catalyzed reaction. Therefore, the $C_6H_{11}O^\bullet$ scavenging studies on cyclohexane oxidation with and without catalyst indicate that $C_6H_{11}O^\bullet$ has only a minor influence on selectivity.

2.4. Spin Trap EPR Measurements. Spin-trap EPR was employed to monitor radicals present in the solution after extended periods of cyclohexane conversion in the reactor for the catalyzed and uncatalyzed reactions. To obtain this information, the spin trap 5,5-dimethyl-1-pyrrolin-N-oxide (DMPO) was added to the reaction solution immediately after extraction from the reactor and filtering off the catalyst. The amount and type of radicals present were then determined from line shape analysis of the resulting EPR spectrum based on spectral simulations (see further details in the SI section "Experimental: spin trap EPR measurements"). This is illustrated in Figure 4, showing the deconvolution of the EPR spectrum after 1 h of cyclohexane oxidation over $LaCo_{0.7}Fe_{0.3}O_3$. Radicals were assigned based on their characteristic hyperfine values a_N and a_H, which determine the number, the spacing and the relative intensities of their

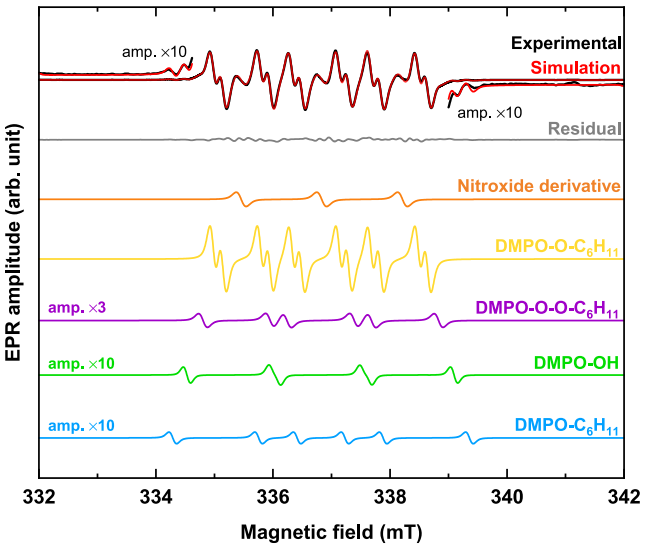

Figure 4. Room temperature spin-trap (DMPO) EPR spectra of the catalyzed reaction after 1 h reaction time. Experimental (black), simulated (red), residual (experiment-simulation, gray). Simulations are a sum of the following radical spectra: di*tert*-butyl-nitroxide derivative (orange), $C_6H_{11}O^\bullet$ (yellow), $C_6H_{11}OO^\bullet$ (purple), $HO^\bullet$ (green) $C_6H_{11}^\bullet$ and (light blue). Reaction conditions: 130 °C, 1.00 mol/L cyclohexane, 20 mg $LaFe_{0.3}Co_{0.7}O_3$, 15 bar O_2, 600 rpm, and 1 h.

https://doi.org/10.1021/acscatal.5c02919
ACS Catal. 2025, 15, 12773−12789

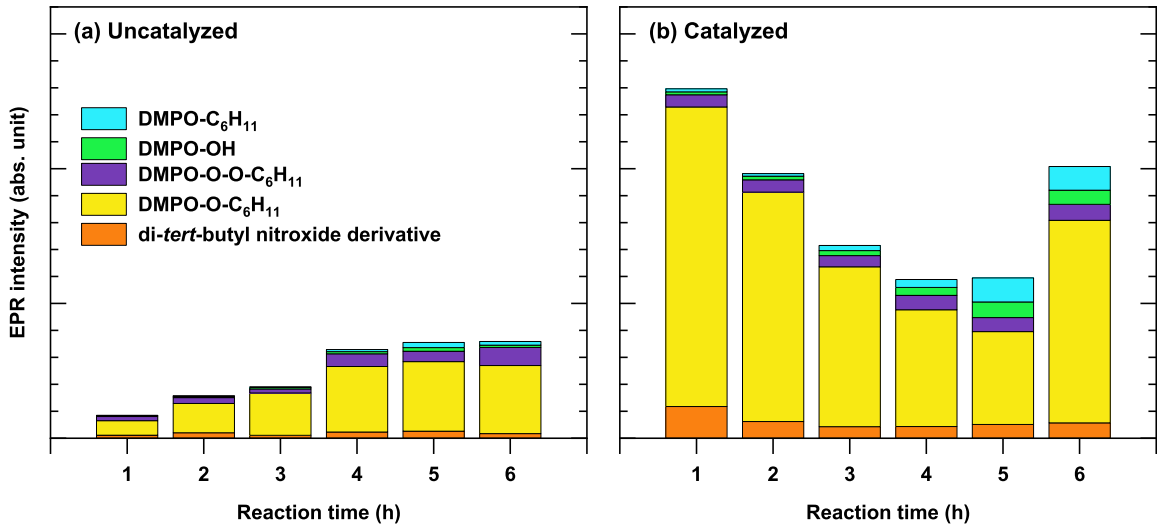

Figure 5. Radical quantities determined using DMPO spin-trap EPR in solutions extracted from the reactor after different reaction times for (a) uncatalyzed and (b) catalyzed reactions. The relative contributions of $C_6H_{11}O^{\bullet}$, $C_6H_{11}OO^{\bullet}$, $C_6H_{11}^{\bullet}$ and $OH^{\bullet}$ are indicated by the color code in the legend. The *y*-axes in (a) and (b) show the same relative radical proportions.

EPR peaks. In accordance with our previous study (Figure S6),[41] the following radicals were identified: $C_6H_{11}O^{\bullet}$ (g_{iso} = 2.0065, a_N = 1.348 mT, $a_{H(\beta)}$ = 0.796 mT, $a_{H(\gamma)}$ = 0.162 mT), $C_6H_{11}OO^{\bullet}$ (g_{iso} = 2.0065, a_N = 1.454 mT, $a_{H(\beta)}$ = 1.142 mT), $C_6H_{11}^{\bullet}$(g_{iso} = 2.0064, a_N = 1.482 mT, $a_{H(\beta)}$ = 2.168 mT), $HO^{\bullet}$ (g_{iso} = 2.0065, a_N = 1.533 mT, $a_{H(\beta)}$ = 1.540 mT), and di-*tert*-butyl-nitroxide derivative (g_{iso} = 2.0064, a_N = 1.372 mT). Double integration (in this case roughly proportional to the peak intensity) over the EPR spectra of the individual radicals give their relative contribution to the total radical amount.

Figure 5 shows the amounts of the trapped radicals in solution extracted from the reactor after reaction times from 1 to 6 h with increments of 1 h without catalyst (Figure 5a) and with catalyst (Figure 5b). Without catalyst, only a small number of radicals is detected after 1 h reaction time, which increases steadily during the first 4 h, with $C_6H_{11}O^{\bullet}$ always accounting for the highest proportion of the radicals produced. After 4 h, the number of radicals stagnates, with the proportion of $C_6H_{11}OO^{\bullet}$ increasing. This time course correlates with a steep increase in cyclohexane conversion (Figure 1) in the first 3 h of the uncatalyzed cyclohexane oxidation and a leveling off of the conversion efficiency between 2 and 4 h, which is accompanied by an increasingly poorer KA oil yield. While the conversion goes up with increasing reaction, the selectivity toward CHHP goes down. As a result, the absolute amount of CHHP is roughly the same for all reaction times.

A completely different scenario was observed in the catalyzed reaction. In this case, the amount of radicals present after 1 h was about ten times higher than in the uncatalyzed case. Again $C_6H_{11}O^{\bullet}$ was the dominant radical. With increasing reaction time, the total amount of radicals decreased sharply between the first and the fifth hour, while the conversion efficiency continued to increase. Under catalytic conditions, the selectivity toward KA oil remained approximately the same during this period. Interestingly, the number of radicals increased again between 5 and 6 h of reaction time, while the selectivity toward KA oil deteriorated and hardly any CHHP could be detected.

Since all samples were subjected to the same procedure after the end of the reaction in the reactor, it is obvious that the differences in the detected radical quantities depend on the different composition of the reaction mixture as a function of the reaction time and the use of a catalyst. However, it must be taken into account that the radicals may both originate directly from the reaction in the reactor or from autoxidation processes in the EPR tube.

Since only a relatively slow increase in the EPR signal was observed within the first hour after addition of the spin trap, autoxidation needs to be taken into account. Previous spin trap EPR studies have shown that cyclohexane autoxidation can be promoted by the addition of CHHP with the formation of $C_6H_{11}O^{\bullet}$, $C_6H_{11}OO^{\bullet}$ and $C_6H_{11}^{\bullet}$.[58,59] We therefore assume that the differences in the amount of radicals captured by DMPO are due to the significant change in the reaction products with and without catalyst and after the respective reaction time, whereby the high proportion of CHHP at the start of the catalyzed reaction appears to contribute significantly to radical formation.[58,59]

2.5. Characterization of the Fresh and Spent Catalyst.

2.5.1. X-ray Diffraction and Rietveld Refinement. XRD was applied prior and after cyclohexane oxidation to investigate the structural changes of the $LaCo_{0.7}Fe_{0.3}O_3$ catalyst. As discussed in the synthesis section, the high level of Co substitution resulted in a minor parasitic spinel fraction (≈ 5%). Thus, the catalytic activity of the $LaFe_{1-x}Co_xO_3$ perovskites might be associated with the parasitic spinel phases present.[41] While the Co_3O_4 spinel phase with Co^{3+} and Co^{2+} cations present in perovskites with $x > 0.3$ might contribute to the overall catalytic activity, it cannot be solely accounted for the catalytic activity because of the improvement in both conversion and KA oil selectivity even at a lower substitution of $x = 0.05$, for which the catalyst is phase-pure without any parasitic spinel phase.

Figure 6 displays the obtained diffractogram of the spent $LaCo_{0.7}Fe_{0.3}O_3$ catalyst. Figure S9a shows the corresponding Rietveld refinement confirming both orthorhombic (PDF 88−0848) and rhombohedral (PDF 88−0641) phases and a minor spinel phase (PDF 42−1467) as also identified in the fresh catalyst. Notably, a new Co-rich layered double hydroxide (LDH) phase was also identified (PDF 500235) around 11.6° 2θ, indicating a possible phase transition of the perovskite in the surface region during cyclohexane oxidation. The broad

https://doi.org/10.1021/acscatal.5c02919
ACS Catal. 2025, 15, 12773−12789

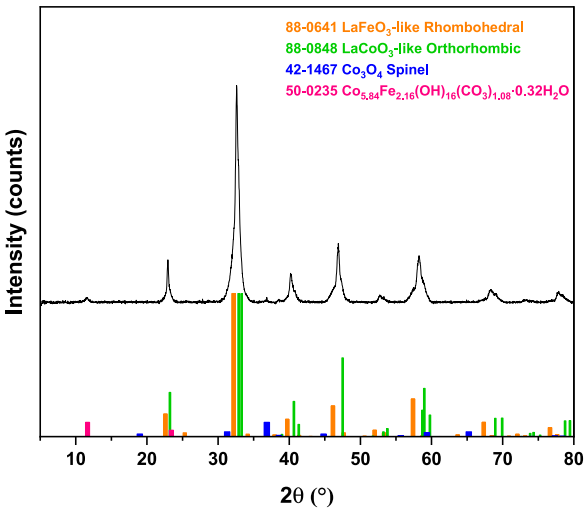

Figure 6. X-ray diffraction pattern of spent $LaCo_{0.7}Fe_{0.3}O_3$.

shoulders exhibited by the spent catalyst suggest a potential phase change, which is further supported by the Rietveld refinement pointing to a transition from the orthorhombic to the rhombohedral phase during cyclohexane oxidation.

The reusability studies using $LaCo_{0.7}Fe_{0.3}O_3$ were reported in our previous work.[41] The results are shown in Figure S9b. Even though a slight decrease in conversion is observed in the third run, the selectivity to KA oil remained very high. To account for leaching and the stability of the catalyst, two additional reusability experiments were performed. In a standard procedure, the reactor was cooled to RT after 6 h of reaction time. The reactor was depressurized and the reaction solution was collected and centrifuged to recover the catalyst. The supernatant solution containing all the reaction components except the catalyst was directly collected for leaching analysis using ICP-MS analysis. Table S4 summarizes the detected amounts of metal species in the reaction sample. No amounts higher than the lower detection limit of 50 ppb were observed. Therefore, leaching was excluded.

In general, Fe^{3+} has an ionic radius of 0.645 Å (high-spin) and 0.55 Å (low-spin) in a 6-fold coordination. Therefore, doping Co^{3+} (0.61 Å high-spin; 0.545 Å low-spin − 6-fold coordinated) into the $LaFeO_3$ lattice should not be a reason for dissolution or migration of ions as the larger or similar-sized Fe^{3+} ions are being replaced by smaller or similar-sized Co^{3+} ions. However, our previous study confirmed that cyclohexane oxidation over $LaCo_xFe_{1-x}O_3$ perovskites proceeds via the reduction of Co^{3+} to Co^{2+} (0.79 Å high-spin; 0.65

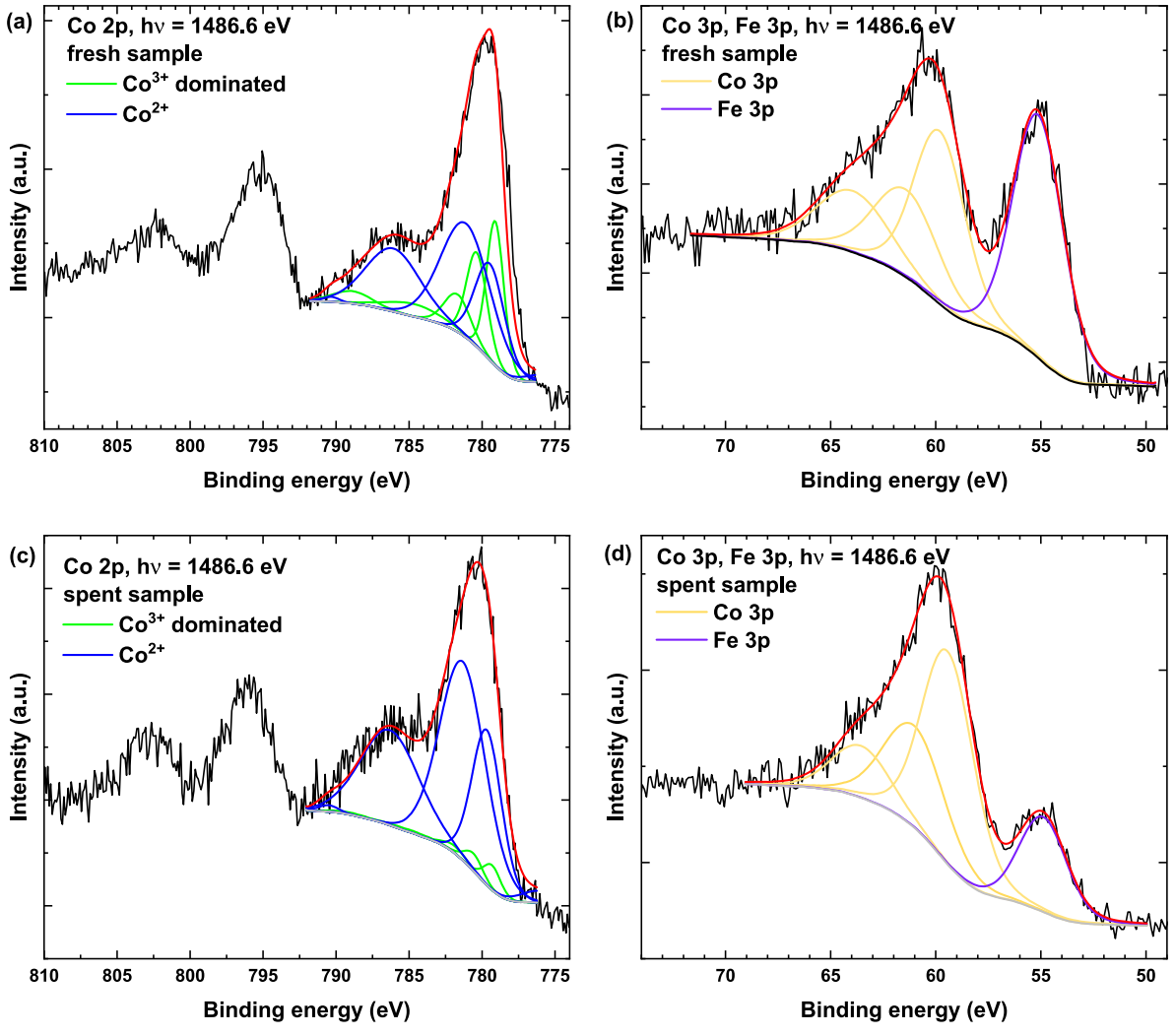

Figure 7. Co 2p (a) and 3p (b) XP spectra of the fresh $LaCo_{0.7}Fe_{0.3}O_3$ and Co 2p (c) and 3p (d) XP spectra of the spent $LaCo_{0.7}Fe_{0.3}O_3$.

https://doi.org/10.1021/acscatal.5c02919
ACS Catal. 2025, 15, 12773−12789

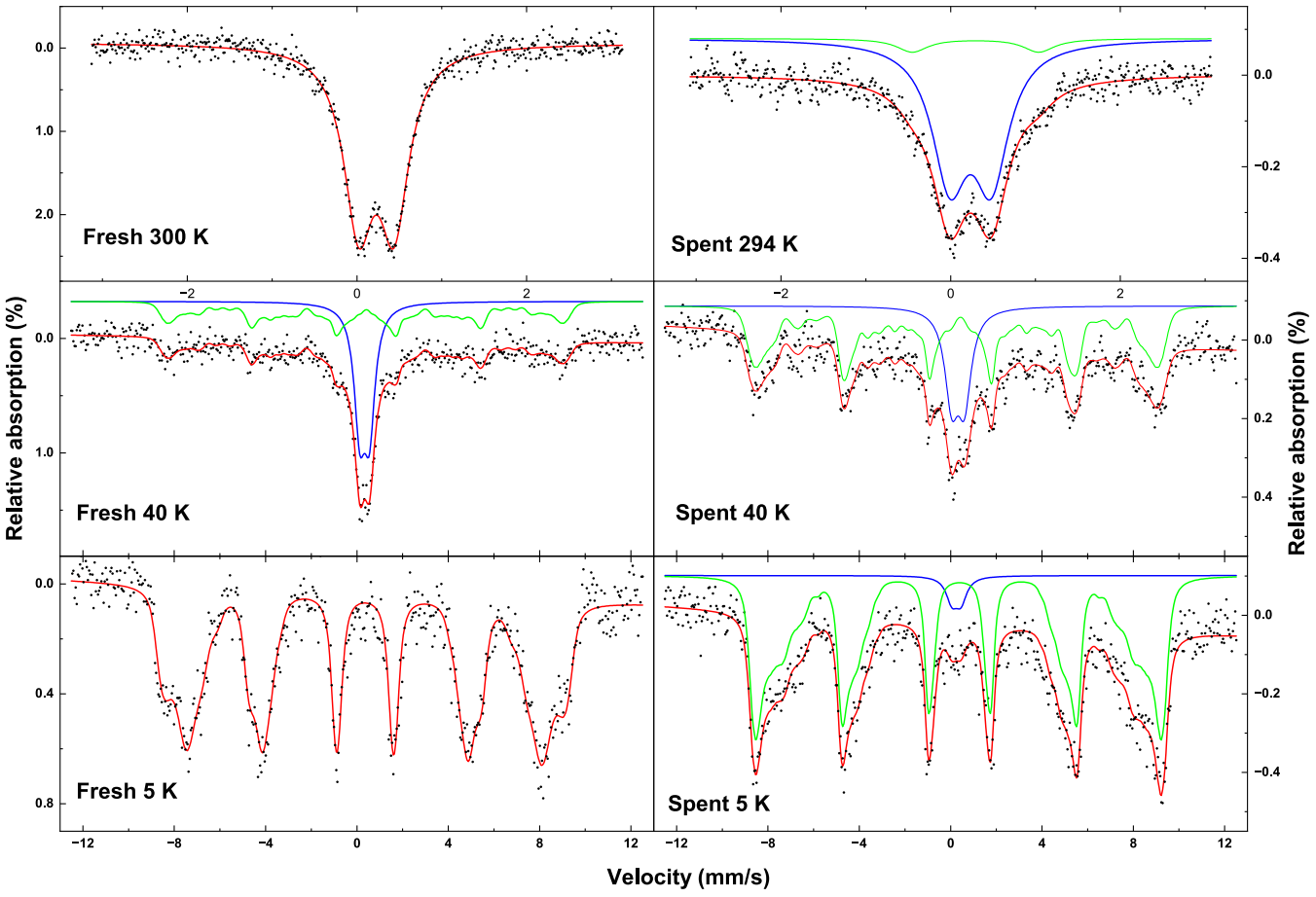

Figure 8. Mössbauer spectra of fresh and spent $LaCo_{0.7}Fe_{0.3}O_3$ recorded at 5, 40 and ≈ 300 K.

Å low-spin − 6-fold coordinated) followed by the reoxidation of the surface, which may result in the formation of new phases during the oxidation reaction.

2.5.2. X-ray Photoelectron Spectroscopy and Temperature-Programmed Reduction. To investigate the surface oxidation states of Co and Fe, XPS measurements were performed as shown in Figure 7. The peak assignment is summarized in Table S5 based on the deconvolution provided in ref.[60] Figure 7a shows the Co 2p spectrum broadened by multiple splitting of the fresh catalyst with both Co^{3+}-dominated and Co^{2+} contributions. The Co^{3+}-dominated contributions (green) appear at 779.1, 780.4, 781.8, 784.9, and 789.2 eV, whereas the Co^{2+} contributions (blue) are at 779.6, 781.4, and 786.4 eV. The Co^{2+} contribution may also originate from the parasitic Co_3O_4 phase in the fresh catalyst in agreement with the XRD measurements. The presence of the satellite peak at 786.4 eV is the major evidence for the presence of Co in the 2+ oxidation state.

Figure 7b shows the Co 2p spectrum of the spent catalyst. The further increase in the Co^{2+} satellite intensity at 786.4 eV confirms our previous findings on the Co^{3+} to Co^{2+} reduction by C−H bond breaking initiation on the catalyst surface.[41] Cyclohexane oxidation over $LaCo_{0.7}Fe_{0.3}O_3$ proceeds via C−H bond breaking and proton-coupled electron transfer (PCET), which results in the reduction of the surface region as supported using H_2 TPR measurements shown in Figure S10. It has to be noted that the expected peaks due to the reduction of the iron component (indicated by arrows in Figure S10) in the H_2 TPR profile are masked by the cobalt component in agreement with literature.[61] Figure 7c,d show the Co and Fe 3p spectra before and after cyclohexane oxidation. As shown in Figure 7d, notable changes of the catalyst surface were observed after cyclohexane oxidation with a strong change in the contribution of Fe^{3+} at 55.4 eV. This result agrees with our XRD observations, where an additional Co-rich LDH-like phase was found. The elemental compositions (at%) of the fresh and spent catalyst are summarized in Table S6. The increase in the Co/Fe ratio of the spent catalyst observed by XPS is in agreement with the newly formed Co-rich LDH-like phase detected by XRD.

Co^{3+} as a dopant in $LaFeO_3$ is feasible in terms of ionic radii in the 3+ oxidation state. However, the reduction of Co^{3+} to Co^{2+} via PCET during cyclohexane oxidation is a crucial step in terms of the structural stability of the catalyst. 6-fold coordinated Co^{2+} (high-spin) has an ionic radius of 0.745 Å, implying that the reduction step results in larger Co^{2+} ions favoring segregation. This step might account for the intensity change of Fe^{3+} at 54.9 eV in the surface-near region probed by XPS. Additionally, as shown by eq 1−3, CHHP decomposition results in water formation as a coupled product. Therefore, the formation of a thin Co-rich LDH layer is also plausible as CHHP decomposition occurs over Co^{2+} (Haber-Weiss reaction).

$$C_6H_{11}OOH + Co^{2+} \rightarrow C_6H_{11}O^{\bullet} + Co^{3+} + HO^{-} \quad (1)$$

$$C_6H_{11}OOH + Co^{3+} \rightarrow C_6H_{11}OO^{\bullet} + Co^{2+} + H^{+} \quad (2)$$

https://doi.org/10.1021/acscatal.5c02919
ACS Catal. 2025, 15, 12773−12789

$$2C_6H_{11}OOH \rightarrow C_6H_{11}O^{\bullet} + C_6H_{11}OO^{\bullet} + H_2O \quad (3)$$

Figure S11 shows the La 3d spectra obtained before (S11a) and after (S11b) cyclohexane oxidation consisting of a core level and a satellite peak at 834.57 and 839.14 eV for the fresh catalyst.[62,63] However, the spent catalyst exhibits an increase in the La^{3+} satellite peak at 838.1 eV.[62,63] The change in satellite intensity for the spent catalyst points to a perturbation in the local electronic environment of La. It could be possible that the reduction of Co^{3+} to Co^{2+} may have also affected La. In case of an incomplete reoxidation of the surface after PCET, it is conceivable that oxygen vacancies are created to maintain the charge balance in the lattice influencing the La^{3+} cations.

Additionally, as shown in Figure S12, the O 1s spectra also indicate significant surface changes that occurred during reaction. The spectrum (Figure S12a) of the fresh catalyst mainly exhibits three peaks at 529.1 eV (O^{2-}, lattice oxygen), 531.0 eV (hydroxyl groups) and 532.4 eV (water).[64] However, for the spent catalyst (Figure S12b), the peak intensity at 529.1 eV is much lower, whereas the peaks at 531.0 and 532.4 eV are much higher, pointing to the formation of a thin Co-rich LDH layer. Figure S13 shows the C 1s spectra where a slight increase in carbonates and carboxylates is observed after cyclohexane oxidation.

2.5.3. Mössbauer Spectroscopy and Magnetometry. Figure 8 shows the Mössbauer spectra of fresh and spent $LaCo_{0.7}Fe_{0.3}O_3$. In general, both samples show a transition from exclusively paramagnetic ordering at room temperature, indicated by the presence of only doublet contributions, to a magnetically ordered sextet structure at low temperature, caused by magnetic hyperfine splitting. Even at room temperature, we can observe clear differences between the two samples: the spectrum of the fresh catalyst requires only one doublet to achieve an appropriate data fit, while the spectrum of the spent catalyst cannot be fully explained by a single doublet contribution. The presence of a second doublet with different isomer shift and quadrupole splitting clearly indicates that the spent catalyst contains Fe ions in two distinct different electronic environments, whereas the original catalyst appears to contain only one Fe-bearing phase. This further confirms the formation of the new Fe-containing phase during cyclohexane oxidation consistent with the XRD and XPS results.

To ensure that there is no influence from any relaxation effects or similar, additional low temperature spectra were recorded, with a temperature of 40 K leading to both catalysts to display a superposition of a magnetically ordered sextet fraction, with the original doublet still being present. Due to the strongly distorted nature of the sextet as well as the high level of noise caused by the low overall Fe content of the samples, we utilized a free distribution magnetic hyperfine field to achieve a satisfactory data fit. Interestingly, there is a clear difference in the ratio between the magnetically ordered and disordered fractions, with the spent catalyst showing a relative sextet spectral area of about 76% compared with 57% of the fresh catalyst. This could point toward a more ferrimagnetic nature of any Fe-containing phase that formed during cyclohexane oxidation, causing a higher degree of magnetic ordering in the spent catalyst. The low temperature spectra also required the use of hyperfine field distributions to properly fit the data at hand, as it was not possible to fully resolve any fine structure of the magnetically blocked phase. Despite this challenge, the two spectra remain distinctly different from each other, with the sextet showing a very different symmetry for either sample, while the spent catalyst retains a minute doublet or singlet fraction even at 5 K. Thus, the overall magnetic character of the sample was strongly altered by cyclohexane oxidation. The spent catalyst displays an overall higher magnetic hyperfine field, potentially indicating the presence of a material of higher magnetic anisotropy. The fresh catalyst exhibits a characteristic sextet indicating magnetic hyperfine splitting,[42] and it exhibits only one characteristic contribution suggesting that only one type of Fe-containing phase is present. The spent catalyst has an additional doublet contribution (shown in blue), which confirms that a new Fe-containing phase has been formed during cyclohexane oxidation in agreement with the XRD and XPS results.

Figure 9 shows the magnetometric measurements carried out at 2 and 300 K to investigate the magnetic ordering of the

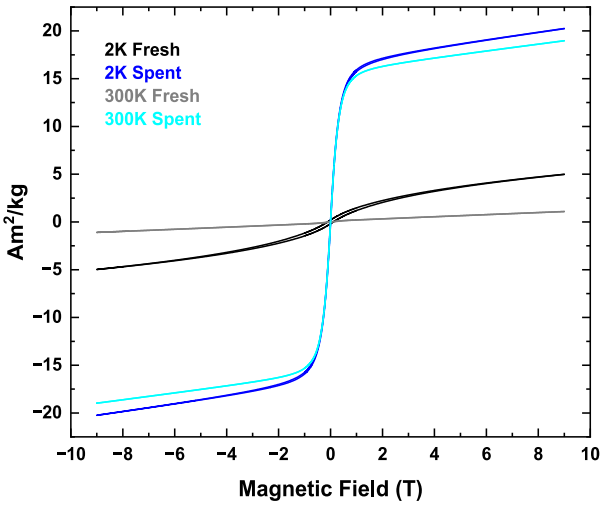

Figure 9. Magnetometry measurements using fresh and spent $LaCo_{0.7}Fe_{0.3}O_3$ at 2 and 300 K.

catalyst. The fresh catalyst exhibits weak ferromagnetic (WFM) behavior, and after catalysis an exponential increase like ferrimagnetic or superparamagnetic-like materials. The high magnetization is usually not observed for $LaCo_xFe_{1-x}O_3$ perovskites but correlating the XRD, XPS, and Mössbauer measurements, this additional phase may be a Co-rich LDH phase containing Fe, as it is reported to show excellent magnetization compared with perovskites.[65,66]

Figure S14 shows the temperature-magnetization relationship for the catalyst both before and after cyclohexane oxidation. Both graphs show a net magnetization and do not approach zero upon heating until 300 K. For the fresh catalyst, the heating−cooling curves coincides within 200−250 K with a net magnetization of 0.036 Am^2/kg at 225 K, which could be described as characteristic of weak ferromagnetic (low magnetization values) materials, since a certain amount of magnetization is maintained even in the absence of an external field. However, the spent catalyst shows a strong increase in the magnetization values (4.45−4.63 Am^2/kg), where the fresh catalyst has values under 0.5 Am^2/kg. This further supports the magnetometry measurements shown in Figure 9, where a clear magnetic phase transition from weakly ferromagnetic to ferrimagnetic was observed. A general trend of decreasing magnetization with cooling is not observed but rather retaining of a residual magnetization (4.54 Am^2/kg) at ≈ 293 K.

https://doi.org/10.1021/acscatal.5c02919
ACS Catal. 2025, 15, 12773−12789

Therefore, the characterization points to a ferrimagnetic material such as the new Co−Fe containing phase formed during cyclohexane oxidation.

2.5.4. EPR Measurements of the Catalysts. Figure 10 shows the EPR spectra of fresh (black) and spent (red)

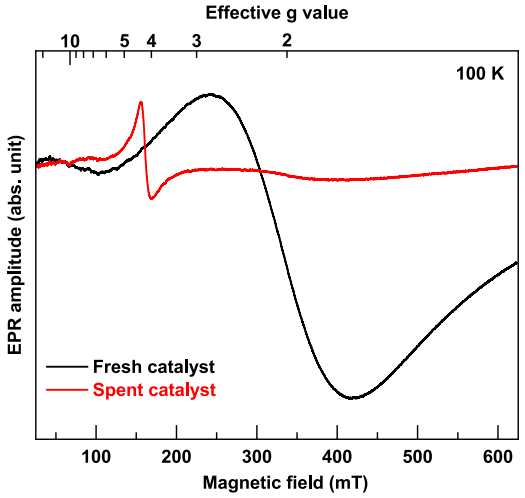

Figure 10. EPR measurements conducted at 100 K using fresh (black curve) and spent (red curve) $LaCo_{0.7}Fe_{0.3}O_3$.

$LaFe_{0.3}Co_{0.7}O_3$ powder samples recorded at 100 K. In the fresh sample, a broad line centered at $g_{eff} \sim 2.1$ was observed. RT Mössbauer spectroscopy on fresh $LaCo_{0.7}Fe_{0.3}O_3$ (Figure 8) revealed a doublet (isomer shift, δ = 0.336 mm/s and quadrupole splitting, Δ = 0.418 mm/s), which split up in a sextet at 5 K ($\delta \sim 0.45$ mm/s, quadrupole shift, $2\varepsilon \sim 0.04$ mm/s, and $H_{hf} \sim 48.95$ T). Both doublet and sextet Mössbauer parameters are in good agreement with values recently reported for $LaCo_xFe_{1-x}O_3$.[61,67] Earlier studies revealed that upon substitution of more than 50% paramagnetic Fe^{3+} with Co^{3+} the antiferromagnetic interaction in $LaFeO_3$ (Néel temperature of 750 K) weakens, thereby lowering the Neel temperature.[61,67] This finding is in accordance with the magnetometry data obtained herein and the observation that the broad $g_{eff} \sim 2.1$ EPR signal was only observed in samples with Co doping above 50% and in the present case strongly decreased in intensity at 5 K. The observed EPR signal is therefore assigned to weakly antiferromagnetically coupled spins at either Fe^{3+} or Co^{2+} located in the $LaFe_{0.3}Co_{0.7}O_3$ phase or in the minority Co_3O_4 phase.

On the contrary, in the spent samples the characteristic EPR signal of distorted rhombic high-spin Fe^{3+} was observed (Figure 10). The same Fe^{3+} signal was observed from room temperature down to 10 K, which indicates that the signal most probably originates from isolated or only weakly coupled Fe^{3+} sites. Similar signals have for example been reported in iron-doped [ZnAl]-layered double hydroxides.[68] In the spent catalyst, XRD (Figure 6) identified new phases in addition to the major $LaCo_xFe_{1-x}O_3$ perovskite phase and the minor spinel phase. The XRD peak at $2\theta = 11.6°$ may indicate the formation of a Co−Fe LDH phase, while the Raman peaks in Figure 11 at 300 cm^{-1} and 683 cm^{-1} are close to the $Co_xFe_{3-x}O_4$ phase. Similar to the fresh samples the RT Mössbauer spectrum of the spent samples was dominated by a doublet and split up to sextets at 5 K. However, in the 5 K

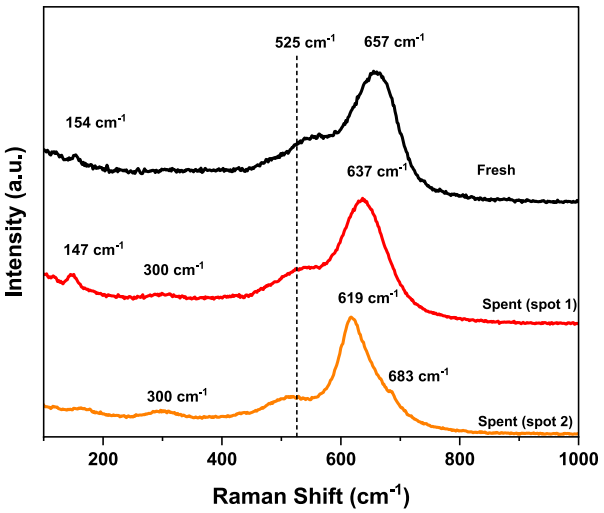

Figure 11. Raman spectra of fresh (black curve) and spent (red-orange curves) $LaCo_{0.7}Fe_{0.3}O_3$.

Mössbauer spectrum of the spent sample an additional small doublet contribution with δ = 0.362 and Δ = 0.40 mm/s appeared, indicating a magnetically isolated Fe^{3+}. This contribution may originate from the same high-spin Fe^{3+} giving rise to the EPR spectrum of the spent samples. This contribution was therefore tentatively assigned to Fe^{3+} in Co−Fe LDH (δ = 0.47 and Δ = 0.50 mm/s at 12 K).[69,70] The presence of the Co−Fe LDH phase also agrees with the results of magnetometry. EPR spectroscopy did not give any evidence for paramagnetic oxygen vacancies at the recording temperatures of 10 K, 100 and 295 K (Figure S23), indicating that oxygen vacancies were either in a diamagnetic state or below the detection limit. Results from different characterization techniques applied herein indicate that the surface of the catalyst undergoes atomic rearrangement during catalysis, whereby Co−Fe-LDH is formed on the one hand and, on the other hand, $Co_xFe_{3-x}O_4$ as detected by Raman spectroscopy.[71,72] It is likely that the drastic differences observed in the EPR spectra of fresh and spent samples result from this atomic rearrangement.

2.5.5. Raman Spectroscopy, TEM, and N_2 Physisorption. Figure 11 shows the Raman spectra obtained with the fresh and spent catalyst. For comparison, the spectra of the reference materials Co_3O_4, CoO and $CoFe_2O_4$ (CFO) are displayed in Figure S15. The fresh $LaCo_{0.7}Fe_{0.3}O_3$ catalyst shows a Raman spectrum that is very similar to the spectrum reported for $LaCoO_3$,[73] with the highest intensity band at 657 cm^{-1}, a broad shoulder between 500 and 600 cm^{-1} and a small band at around 154 cm^{-1}. The band at 657 cm^{-1} has been assigned to the E_g stretching vibration in the rhombohedral phase where the contribution to the scattering intensity is due to the population of undistorted CoO_6 octahedra with Co^{3+}.[73]

Two representative spectra that were recorded on two different spots of the spent catalyst are also shown in Figure 11. These spectra typically show a broad band with the highest relative intensity at a position ranging from 619 − 637 cm^{-1} accompanied by a broad shoulder between 450 and 550 cm^{-1} as well as broad bands with low intensity at 300 cm^{-1}. The highest intensity band can be regarded as shifted toward lower wavenumbers compared with the one observed for the fresh sample. At spot 1, the band with the highest intensity is situated at 637 cm^{-1}, whereas an additional small band at 147

https://doi.org/10.1021/acscatal.5c02919
ACS Catal. 2025, 15, 12773−12789

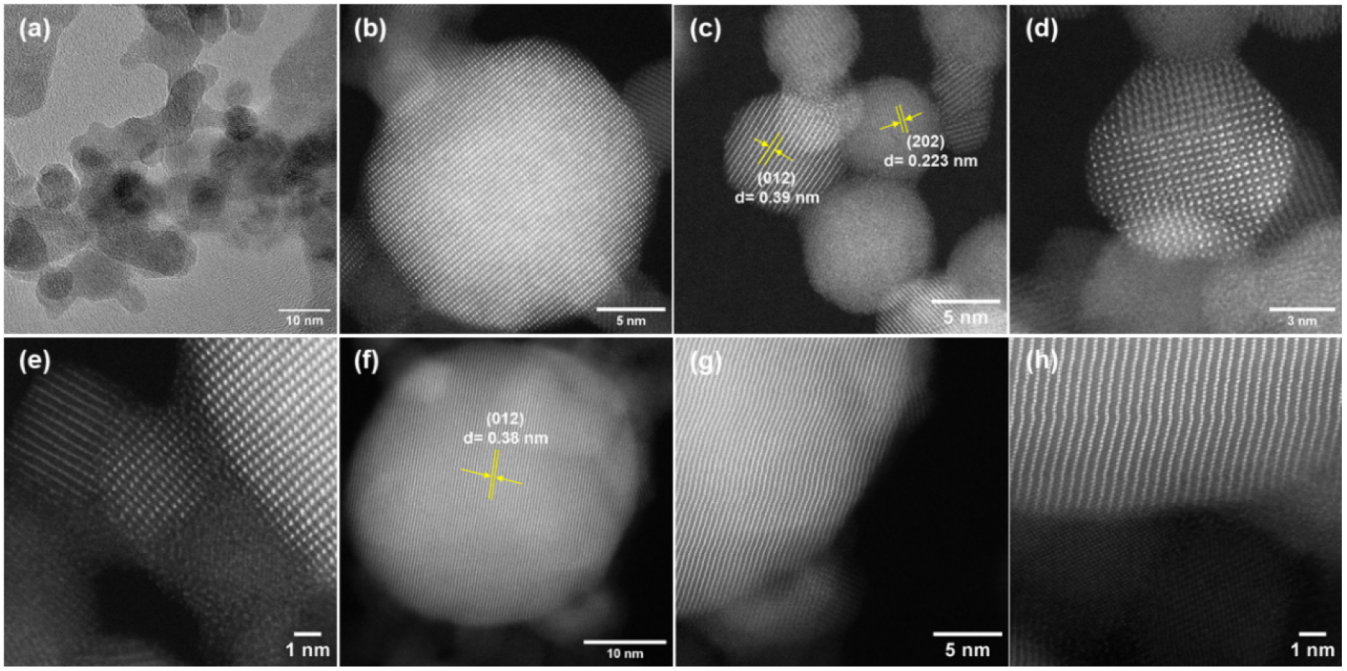

Figure 12. TEM images of fresh (a-d) and spent (e-h) $LaCo_{0.7}Fe_{0.3}O_3$.

cm^{-1} was detected in very good agreement with results previously published for $LaCo_{0.2}Fe_{0.8}O_3$,[74] i.e., a $LaCo_xFe_{1-x}O_3$ material with a low Co:Fe ratio. At spot 2, the band with the highest intensity is shifted further to lower wavenumbers, i.e., 619 cm^{-1}, a position which is typical for bands observed for $LaFeO_3$,[75,76] i.e., La perovskites without Co. In normal $LaFeO_3$, however, an additional band with high intensity should be present between 400 and 450 cm^{-1}, which is absent in our spectra. DFT calculations have shown that $LaFeO_3$ with oxygen vacancies does not show this band either.[76] Therefore, in the spent sample, part of the Co ions seems to have been removed from the perovskite lattice, leading to a $La-Co_xFe_{1-x}O_3$ perovskite with a lower Co:Fe ratio.

The formation of a new Co-containing phase such as CoO or $CoFe_2O_4$ is difficult to deduce from the spectra. Although in defect-free CoO single crystals, the first-order phonon Raman scattering is forbidden according to the selection rules for the NaCl-type centrosymmetric lattice structure,[77] it is known that defective CoO shows a broad band centered at around 530 cm^{-1}.[78,79] This was confirmed by a reference CoO sample shown in Figure S15. All the spectra show broad features around 530 cm^{-1}. Moreover, the presence of $CoFe_2O_4$ may be indicated by broad bands at 300 cm^{-1} and 684 cm^{-1} (Figure S15), which are also present in the spectra. However, all these features are also characteristic for the perovskites. Therefore, the presence of CoO and/or $CoFe_2O_4$ in the spent sample can neither be excluded nor confirmed directly by Raman spectroscopy.

To investigate the morphological changes, high-resolution transmission electron microscopy (HR-TEM) measurements were carried out using the fresh and the spent catalyst as shown in Figure 12a-h. The images seem to be comparable and do not indicate any strong structural changes. Furthermore, the distinct 0.38 nm (012) lattice fringes of $LaCoO_3$ were preserved, confirming the overall maintenance of structural integrity.[80,81] N_2 physisorption measurements (Figure S16) confirm that the surface areas as well as the pore sizes are rather similar in the fresh and the spent catalyst amounting to 18.2 m^2/g and 8.2 nm and 15.3 m^2/g and 8.0 nm in the fresh and spent catalyst, respectively.

2.6. CoO as Catalyst and TBHP Decomposition. To investigate the catalytic influence of Co^{2+}, a commercial Co(II) oxide (CoO) catalyst was applied in the oxidation reaction. The phase purity of the material was confirmed using XRD as shown in Figure S17. The material was referenced to the diffractogram of Co(II)O (PDF 98−000−9865). To check for Co_3O_4, a reference spectrum (PDF 98−002−7498) was used and found to be absent. The average particle size was approximately between 30 and 50 nm, and the CoO sample was used as such. The reactions were conducted under milder conditions of 120 °C, 1.00 mol/L, and 15 bar O_2 to observe the catalytic efficiency in overcoming the induction period. The results shown in Figure 13 were then compared to reactions with and without $LaCo_{0.7}Fe_{0.3}O_3$ as catalyst.

As shown in Figure S2, the uncatalyzed reaction is associated with a 2 h induction period and achieves a conversion of 3.3% after 6 h, and CHHP remains at 35% after 6 h suggesting an incomplete decomposition. Figure 13 shows that using CoO as catalyst did not influence the initiation of the reaction significantly: despite an increase in conversion ($X \approx 7\%$), the induction period remained the same (≈ 2 h). However, the CHHP intermediate decomposed to a significantly higher extent compared with the uncatalyzed reaction. After 6 h, only 5.2% selectivity to CHHP was observed and a higher KA oil selectivity was achieved, pointing to the strong effect of Co^{2+} on the decomposition of the formed hydroperoxide. The unchanged induction period further confirms that Co^{2+} is not involved in the initiation step but rather in the propagation by CHHP decomposition to KA oil. As shown in Figure S2b, $LaCo_{0.7}Fe_{0.3}O_3$ as catalyst reduces the induction period to less than 1 h at 120 °C with a considerably higher degree of conversion ($X \approx 15\%$) after 6 h, confirming that free radical generation during initiation requires Co^{3+} surface sites according to the hypothesis of a PCET reaction at the surface

https://doi.org/10.1021/acscatal.5c02919
ACS Catal. 2025, 15, 12773−12789

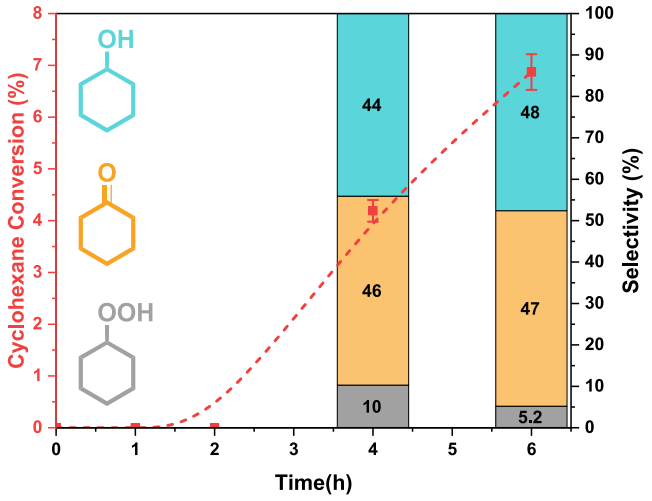

Figure 13. Conversion-selectivity profile of cyclohexane oxidation over CoO. Reaction conditions: 120 °C, 1.00 mol/L cyclohexane, 20 mg CoO, 15 bar O_2, 600 rpm, 6 h, acetonitrile as solvent, and biphenyl as internal standard.

based on La−Co^{3+}-O^{2-} sites.[41] While Co^{2+} accelerates CHHP decomposition, Co^{3+} is required for the free radical generation by C−H bond dissociation through PCET. Therefore, the catalyst is assumed to play a dual role in the liquid-phase oxidation of cyclohexane.

A kinetic investigation based on the postulated ability of Co^{2+} to decompose the hydroperoxide intermediate was carried out (Figure S18). Figure S18a shows a setup to measure evolved gas volumes in which *tert*-butyl hydroperoxide (TBHP) is decomposed to *tert*-butanol and O_2. The quantification of evolved O_2 can then be correlated to the ability of the catalyst to decompose hydroperoxide intermediates. As Figure S18b shows, a blank reaction only with TBHP at 50 °C yields less than 0.5 mL O_2 after 6 h. Upon adding $LaFeO_3$, the amount of evolved O_2 increased to 1 mL indicating a poor increase in the decomposition rate. A notable increase to 2.5 mL is exhibited by $LaFe_{0.95}Co_{0.05}O_3$ (x = 0.05) after 6 h. These two observations can be correlated with the activity in cyclohexane oxidation, where an increase in conversion was exhibited by $LaFe_{0.95}Co_{0.05}O_3$ (x = 0.05) while $LaFeO_3$ remained inactive. At x = 0.7, the evolved O_2 volume is around 3.5 mL suggesting a positive influence of Co substitution in hydroperoxide decomposition. The catalyst (x = 0.7) after cyclohexane oxidation was recovered to investigate TBHP decomposition. The spent catalyst reached a significant increase of 2.5 mL relative to the fresh catalyst in the evolved O_2 amount. As reference, CoO was used as a catalyst in TBHP decomposition, exhibiting the highest amount of O_2 amounting to 7 mL after 6 h. Therefore, the TBHP decomposition experiments clearly show that Co^{2+} has a higher activity than Co^{3+} in hydroperoxide decomposition. Correspondingly, the spent catalyst exposes a higher amount of Co^{2+} than the fresh catalyst in agreement with the characterization results.

2.7. Mechanistic Analysis. Figure S19 illustrates the proposed reaction network, which proceeds through a PCET at the surface.[41] The homolytic C−H bond cleavage of cyclohexane initiates the reaction forming an electron and a proton. La^{3+} is bound to lattice oxygen (O^{2-}) making it relatively more basic. The basicity of O^{2-} enables it to accept the proton generated by the C−H bond cleavage transforming into OH^-, and Co^{3+} is reduced to Co^{2+} by the electron. As observed in using CoO as catalyst and in TBHP decomposition, the newly formed Co^{2+} ions facilitate the CHHP decomposition to produce KA oil. Therefore, the catalytic activity is mainly attributed to the Co^{3+}/Co^{2+} redox pair, where Co^{3+} enables initiation and Co^{2+} catalyzes CHHP decomposition. Ideally, the subsequent reoxidation regenerates the initial state of the catalytically active surface. However, it was observed in this study that the catalyst undergoes a phase transition in the surface region induced by reduction, resulting in Co^{2+} segregation. Due to the catalytically inert $LaFeO_3$ sample, Fe^{3+} ions were not included in the reaction network. As discussed before, reduction of Co^{3+} to Co^{2+} can alter the structure in different ways. Based on a Co^{3+}-O^{2-}-Fe^{3+} surface (as in $LaCo_{0.7}Fe_{0.3}O_3$), it has to be speculated that changes in Co oxidation states can lead to the formation of a Co-rich LDH phase containing the formed Co^{2+} ions present as a thin film on the perovskite bulk.

Radical scavenging studies showed that controlling the $C_6H_{11}OO^\bullet$ population favors KA oil selectivity (Figure 3). The $C_6H_{11}OO^\bullet$ radical is highly oxidizing and dominates the uncatalyzed reaction (Figure 15).[41] The decrease in KA oil selectivity (Figure 1a) is primarily due to the overoxidizing nature of $C_6H_{11}OO^\bullet$. When these radicals are scavenged (Figure 3), the KA oil selectivity is significantly improved. As the catalyst also favored KA oil selectivity and $C_6H_{11}OO^\bullet$ is highly reactive, it may react further with the catalyst surface. A plausible catalytic cycle is shown in Figure 14, where the rapid

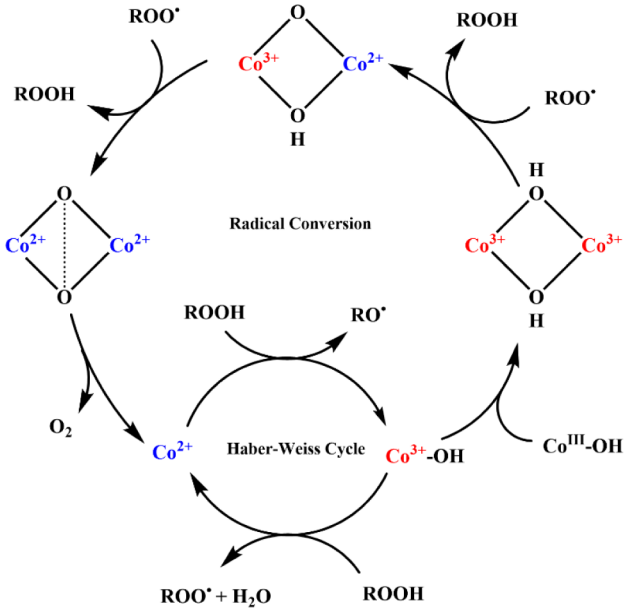

Figure 14. Postulated catalytic cycle for rapid conversion of highly oxidizing $C_6H_{11}OO^\bullet$ to CHHP via Co-based oxyhydroxy moieties.

conversion of $C_6H_{11}OO^\bullet$ to CHHP and KA oil takes place on two coupled Co sites. Based on the PCET mechanism (Figure S19), the reduction of the surface generates Co^{2+} sites which further participate in the Haber-Weiss reaction.[41] The generated Co^{3+}/Co^{2+} redox pair can in parallel form oxyhydroxy moieties that rapidly convert overoxidizing $C_6H_{11}OO^\bullet$ back to CHHP, thereby favoring KA oil selectivity.

Co^{2+} decomposes the CHHP intermediate via homolytic cleavage of the -OOH bond forming $C_6H_{11}O^\bullet$ and Co^{3+}−OH

https://doi.org/10.1021/acscatal.5c02919
ACS Catal. 2025, 15, 12773−12789

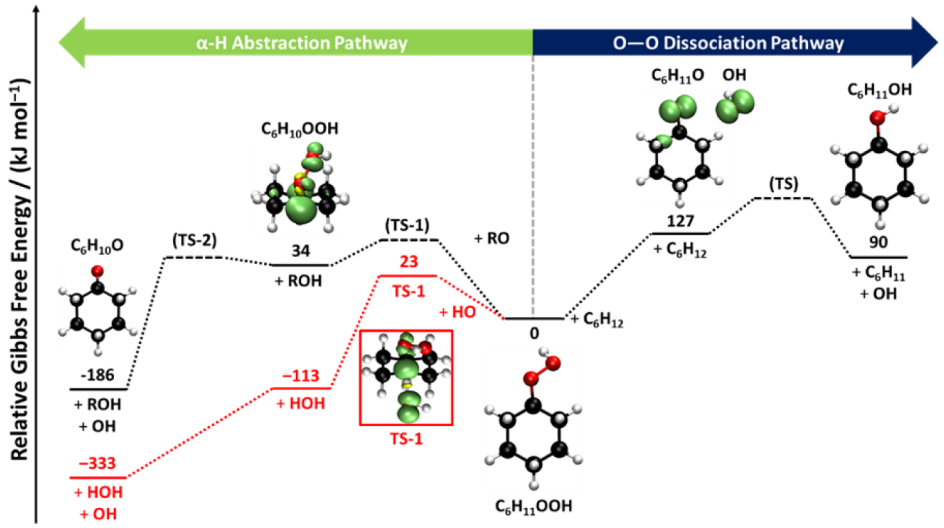

Figure 15. Energy diagram for the α-H abstraction (left) vs O−O dissociation (right) pathways of CHHP ($C_6H_{11}OOH$). For the α-H abstraction, paths for $R = C_6H_{11}O$ (black) and $R = H$ (red) are included. Verified transition states (TS) are shown as solid lines and hypothesized ones as dashed lines. The electron spin density is included as contour lines (plotted at isovalues of ± 0.01). All energies refer to relative Gibbs free energies in solution in 95 mol % acetonitrile at 130 °C with 5 mol % of C_6H_{12}.

(surface). Two adjacent surface Co^{3+}−OH dimerize to form a proton-rich oxyhydroxy-like entity. $C_6H_{11}OO^{\bullet}$ abstracts the protons to rapidly form CHHP leading to deprotonation of the entity. The Co-$(O)_2$-Co peroxo complex further dissociates to regenerate the surface releasing molecular oxygen. The presence of similar entities on a heterogeneous catalytic surface has been widely investigated in the oxygen evolution reaction[82] as well as in water splitting.[83,84] Homogeneous (bulk) reactions also support the formation of such complexes in oxidation and deperoxidation reactions.[85]

Figure S20 illustrates that CHHP decomposition can occur via both O−O homolytic cleavage as well as the α-H abstraction pathway. The homolytic O−O cleavage generates more $C_6H_{11}O^{\bullet}$ and $HO^{\bullet}$, whereas previous reports describe that uncatalyzed reactions mostly proceed via the α-H abstraction pathway as it is highly favorable due to abundant $C_6H_{11}OO^{\bullet}$ at initiation. The choice of the pathway is mainly influenced by the stability of the generated radicals. The $C_6H_{11}OO^{\bullet}$ radicals have relatively higher stabilization due to the resonance effect of the peroxyl group ($OO^{\bullet}$). Consequently, the unpaired electron is less available for reaction due to delocalization. Additionally, the adjacent C−H bond further stabilizes the radical by hyperconjugation. Studies on the gas-phase oxidation of cyclohexane found an enthalpy difference between $C_6H_{11}OO^{\bullet}$ and $C_6H_{11}O^{\bullet}$ of about 15 kJ/mol.[86]

Using a combination of COSMO-RS, DFT, and highly accurate explicitly correlated CCSD(T) calculations, we determined the Gibbs free energies in solution (95 mol % acetonitrile, 5 mol % C_6H_{12}, 130 °C) for the α-H abstraction and O−O dissociation pathways as summarized in Figure 15. The homolysis of $C_6H_{11}OOH$ into $C_6H_{11}O^{\bullet}$ and $^{\bullet}OH$ proceeds barrier-less but is energetically unfavored (127 kJ/mol). In contrast, the α-H abstraction at $C_6H_{11}OOH$ appears to have a small activation barrier (e.g., 17 kJ/mol for $R = OH$), leading to a reactive $C_6H_{10}OOH$ intermediate that is only slightly higher in energy (e.g., 34 kJ/mol for $R = C_6H_{11}O$), but which readily undergoes a strongly exergonic (barrierless) decomposition into cyclohexanone and OH. Thus, these results suggest that under mild reaction conditions as well as in uncatalyzed reactions, α-H abstraction is predominant. However, in the presence of a suitable catalyst, the O−O cleavage dominates and generates more $C_6H_{11}O^{\bullet}$.

3. CONCLUSION

Co-substituted $LaFeO_3$ ($LaCo_{0.7}Fe_{0.3}O_3$) perovskite nanoparticles were applied as catalyst in the liquid-phase oxidation of cyclohexane using molecular oxygen to KA oil, which achieved promising results under mild reaction conditions (120 °C) with a high KA oil selectivity of 95% at X ≈ 15%. While the uncatalyzed reaction yielded byproducts with 79% selectivity (X ≈ 24%), the catalyzed reaction achieved around 63% KA oil (X ≈ 37%) after 6 h at 130 °C. It was observed that the catalyst improved the stability of KA oil especially at high conversion. *In situ* ATR-IR spectroscopy enabled the visualization of the differences in product distribution in both reactions. Radical scavenging studies confirmed the highly oxidizing nature of $C_6H_{11}OO^{\bullet}$ causing overoxidation of KA oil in uncatalyzed reactions. EPR spin trap measurements using DMPO showed that $C_6H_{11}O^{\bullet}$ radicals are dominant in catalyzed reactions, in which $C_6H_{11}OO^{\bullet}$, $C_6H_{11}^{\bullet}$ and $HO^{\bullet}$ were also identified. Quantum chemical calculations revealed that CHHP decomposition is favored via the α-H abstraction pathway in the absence of a catalyst yielding $C_6H_{11}O^{\bullet}$. Higher KA oil selectivity is assumed to be correlated with the switch in the radical population from highly oxidizing $C_6H_{11}OO^{\bullet}$ to mildly oxidizing $C_6H_{11}O^{\bullet}$ in the catalyzed reaction. Post-catalytic characterization confirmed a reduction of Co^{3+} to Co^{2+} in the near-surface region during cyclohexane oxidation. Mössbauer spectroscopy provided evidence that a new Co-rich LDH phase was present presumably as thin layer on the spent catalyst as further supported by XRD, EPR measurements of the catalysts and magnetometry measurements. Using Co(II)O as catalyst confirmed that Co^{2+} is mainly involved in CHHP decomposition and not in initiation. Therefore, the Co^{3+}/Co^{2+} redox pair is identified to be responsible for the overall catalytic activity. Based on these findings, a catalytic cycle was proposed in which the highly oxidizing $C_6H_{11}OO^{\bullet}$ radicals are

https://doi.org/10.1021/acscatal.5c02919
ACS Catal. 2025, 15, 12773−12789

rapidly converted to CHHP via proton-rich oxyhydroxy-like species formed in parallel by the Haber-Weiss cycle. The combined use of experimental and computational approaches highlights the key role of the catalyst in controlling the radical pathway, leading to improved KA oil selectivity and stability.

3.1. Methods. *3.1.1. Materials.* For the synthesis of $LaCo_{0.7}Fe_{0.3}O_3$, commercial reagents were used as such: iron(III) nitrate nonahydrate (≥98%, SigmaAldrich GmbH, Germany), cobalt(II) nitrate hexahydrate (≥98%, Carl Roth GmbH, Germany), lanthanum(III) nitrate hexahydrate (99.9% La, abcr GmbH, Karlsruhe, Germany), sodium carbonate (≥99.5%, VWR International GmbH, Germany), sodium hydroxide (98.5% Carl Roth GmbH, Germany). Co(II)O used as a benchmark in cyclohexane oxidation and TBHP decomposition (≥99.5%, Merck).

For cyclohexane oxidation: cyclohexane (99%, VWR International GmbH, Germany) and acetonitrile (in analytical range grade, SigmaAldrich GmbH, Germany), cyclohexanol (99%), cyclohexanone (99%), 7-oxabicyclo[4.1.0]heptane-2-one (98%), Biphenyl (99%) from Sigma-Aldrich GmbH, Germany. Cyclohexane1,2diol (98%), cyclohexane1,2dione (98%), Cyclohexane1,4diol (98%), cyclohexane1,4dione (98%) from Fischer Scientific GmbH, Germany. For radical scavenging studies: 2,2,6,6tetramethylpiperidinooxy (TEMPO, 98%), 2-methylpropan2ol (*tert*butanol, 99.5%), 1,4-benzoquione (*p*-benzoquinone, 98%) from Sigma-Aldrich GmbH, Germany. For EPR measurements: 5,5-dimethyl-1-pyrroline-N-oxide (DMPO, 98%) from SigmaAldrich GmbH, Germany. For TBHP decomposition: 2-hydroperoxy-2-methylpropane (70 wt % in water) from Sigma-Aldrich GmbH, Germany. All reagents were used without further purification.

3.1.2. Catalyst Synthesis. $LaCo_{0.7}Fe_{0.3}O_3$ was synthesized according to our previous studies.[41,42] For precipitation, a solution containing 1.2 M NaOH and 0.18 M Na_2CO_3 was used. The synthesis was carried out in a single-walled glass reactor from Mettler Toledo GmbH equipped with a thermostat. The experiments were conducted at a constant pH of 9.5 and isothermally at 10 °C. Dosing rate of the metal salt solution was kept at 2.08 g/min by using a universal control box. An impellor at 300 rpm confirmed the homogeneity of the mixture. An aging procedure at 10 °C for 60 min followed the precipitation. The mixture was then centrifuged at 6000 rpm for 2 min to isolate the precipitate. To remove the hydroxide and carbonates, washing was performed until the supernatant had a conductivity below 0.1 mS/cm. The washing followed a drying procedure (overnight, 12 h) at 80 °C which were then calcined at 800 °C for 3 h.

3.1.3. Catalytic Oxidation Reactions. Cyclohexane oxidation was carried out in a 160 mL batch stainlesssteel reactor 4560 from Parr instruments operable up to 60 bar and equipped with Teflon liner. The standard reaction conditions were set at 130 °C, 15 bar O_2, 1.00 mol/L cyclohexane in acetonitrile, 600 rpm and 6 h. To a solution containing 40 mL acetonitrile and 40 mmol of cyclohexane, 20 mg catalyst were dispersed. About 1.00 mmol of biphenyl was added as the internal standard for GC analysis. Directly after transferring to the vessel, the reactor was tightened and sealed followed by flushing with O_2 three times. The desired pressure of 15 bar was set afterward, and the system was heated to 130 °C. Once the set temperature was reached, the stirring started to initiate the reaction. Sampling (0.5 mL) was done after filtering (syringe filter, 200 nm) off the catalyst after 1, 2, 4, and 6 h of reaction time where two samples were taken per withdrawal. One was measured as such, and the other was treated with 2 mmol triphenylphosphine to reduce CHHP to cyclohexanol. The CHHP intermediate was then quantified using the difference between the cyclohexanol amount between the two samples. The reproducibility of the experiment was ensured with a deviation below 5%. For the radical scavenging experiments, all the standard conditions were kept as such and 2 mol % of the scavenger were added to the reaction mixture at the beginning. Within the operating conditions, acetonitrile was found to be inert and did not react with the generated free radicals.

Details of the spin trap EPR measurements, the postcatalytic characterization and the quantum chemical calculations can be found in the Supporting Information.

■ ASSOCIATED CONTENT

Supporting Information

The Supporting Information is available free of charge at https://pubs.acs.org/doi/10.1021/acscatal.5c02919.

XRD Rietveld analysis, EPR measurements, radical scavenging studies, ICP-MS, XPS spectra, temperature-magnetization curves, Raman spectra, TBHP decomposition, experimental details of postcatalytic characterization and quantum chemical calculations. Molecular structures together with their HF energies(PDF)

■ AUTHOR INFORMATION

Corresponding Authors

Martin Muhler − *Laboratory of Industrial Chemistry, Ruhr University Bochum, Bochum 44780, Germany; Max Planck Institute for Chemical Energy Conversion, Mülheim an der Ruhr 45470, Germany;* orcid.org/0000-0001-5343-6922; Email: martin.muhler@ruhr-uni-bochum.de

Alexander Schnegg − *Max Planck Institute for Chemical Energy Conversion, Mülheim an der Ruhr 45470, Germany;* orcid.org/0000-0002-2362-0638; Email: alexander.schnegg@cec.mpg.de

Authors

Akhil Hareendran − *Laboratory of Industrial Chemistry, Ruhr University Bochum, Bochum 44780, Germany*

Takuma Sato − *Max Planck Institute for Chemical Energy Conversion, Mülheim an der Ruhr 45470, Germany*

Maik Dreyer − *Institute of Inorganic Chemistry, Kiel University, Kiel 24118, Germany*

Anna Rabe − *Faculty of Physics and Center for Nanointegration Duisburg-Essen (CENIDE), University of Duisburg-Essen, Duisburg 47057, Germany*

Soma Salamon − *Faculty of Physics and Center for Nanointegration Duisburg-Essen (CENIDE), University of Duisburg-Essen, Duisburg 47057, Germany;* orcid.org/0000-0002-8661-6038

Niklas Sülzner − *Chair of Theoretical Chemistry, Ruhr University Bochum, Bochum 44780, Germany;* orcid.org/0000-0002-8734-5807

Ulrich Hagemann − *Interdisciplinary Center for Analytics on the Nanoscale (ICAN) and Center for Nanointegration Duisburg-Essen (CENIDE), University of Duisburg-Essen, Duisburg 47057, Germany;* orcid.org/0000-0002-1880-6550

Catalina Leiva-Leroy − *Laboratory of Industrial Chemistry, Ruhr University Bochum, Bochum 44780, Germany*

https://doi.org/10.1021/acscatal.5c02919
ACS Catal. 2025, 15, 12773−12789

Nicolas Cosanne − *Institute of Inorganic Chemistry, Kiel University, Kiel 24118, Germany*
Krishnan Ravi − *Laboratory of Industrial Chemistry, Ruhr University Bochum, Bochum 44780, Germany;* orcid.org/0000-0002-4656-5221
Dongsheng Zhang − *Laboratory of Industrial Chemistry, Ruhr University Bochum, Bochum 44780, Germany*
G. Wilma Busser − *Laboratory of Industrial Chemistry, Ruhr University Bochum, Bochum 44780, Germany*
Malte Behrens − *Institute of Inorganic Chemistry, Kiel University, Kiel 24118, Germany;* orcid.org/0000-0003-3407-5011
Christof Hättig − *Chair of Theoretical Chemistry, Ruhr University Bochum, Bochum 44780, Germany;* orcid.org/0000-0002-5752-2710
Heiko Wende − *Faculty of Physics and Center for Nanointegration Duisburg-Essen (CENIDE), University of Duisburg-Essen, Duisburg 47057, Germany;* orcid.org/0000-0001-8395-3541

Complete contact information is available at: https://pubs.acs.org/10.1021/acscatal.5c02919

Notes

The authors declare no competing financial interest.

■ ACKNOWLEDGMENTS

This research was funded by the Deutsche Forschungsgemeinschaft (DFG, German Research Foundation, project number 388390466 TRR 247). We thank Dr. Frank Girgsdies and Dr. Wulyu Jiang (Fritz Haber Institute (FHI), Berlin) for the XRD measurements and the Rietveld analysis. We thank Dr. Markus Heidelmann (Interdisciplinary Center for Analytics on the Nanoscale (ICAN), University of DuisburgEssen) for the HR-TEM measurements. Mrs. Noushin Arshadi is acknowledged for the TPR and N_2 physisorption measurements. This work was supported by the "Center for Solvation Science ZEMOS" funded by the German Federal Ministry of Education and Research (BMBF) and by the Ministry of Culture and Research of North Rhine-Westphalia.

■ REFERENCES

(1) Goel, P.; Sundriyal, S.; Shrivastav, V.; Mishra, S.; Dubal, D. P.; Kim, K.-H.; Deep, A. Perovskite materials as superior and powerful platforms for energy conversion and storage applications. *Nano Energy* **2021**, *80*, 105552.
(2) Wang, Z.; Wang, Y.; Wang, J.; Song, Y.; Robson, M. J.; Seong, A.; Yang, M.; Zhang, Z.; Belotti, A.; Liu, J.; Kim, G.; Lim, J.; Shao, Z.; Ciucci, F. Rational design of perovskite ferrites as high-performance proton-conducting fuel cell cathodes. *Nat. Catal.* **2022**, *5* (9), 777−787.
(3) Arandiyan, H.; Sudarsanam, P.; Bhargava, S. K.; Lee, A. F.; Wilson, K. Perovskite Catalysts for Biomass Valorization. *ACS Catal.* **2023**, *13* (12), 7879−7916.
(4) Voorhoeve, R. J.; Johnson, D. W.; Remeika, J. P.; Gallagher, P. K. Perovskite oxides: materials science in catalysis. *Science* **1977**, *195* (4281), 827−833.
(5) Riisnaes, K. J.; Alshehri, M.; Leontis, I.; Mastria, R.; Lam, H. T.; De Marco, L.; Coriolano, A.; Craciun, M. F.; Russo, S. 2D Hybrid Perovskite Sensors for Environmental and Healthcare Monitoring. *ACS Appl. Mater. Interfaces* **2024**, *16* (24), 31399−31406.
(6) Capdevila-Cortada, M. Describing perovskite catalysts. *Nat. Catal.* **2018**, *1* (10), 737.
(7) Gu, J.; Li, F.; Wang, Z.; Xie, Y.; Yan, L.; Zeng, P.; Yu, H.; Liu, M. Morphology Tuning and Its Role in Optimization of Perovskite Films Fabricated from A Novel Nonhalide Lead Source. *Adv. Sci.* **2020**, *7* (23), 2002296.
(8) Zuo, L.; Dong, S.; De Marco, N.; Hsieh, Y.-T.; Bae, S.-H.; Sun, P.; Yang, Y. Morphology Evolution of High Efficiency Perovskite Solar Cells via Vapor Induced Intermediate Phases. *J. Am. Chem. Soc.* **2016**, *138* (48), 15710−15716.
(9) Chen, H.; Lim, C.; Zhou, M.; He, Z.; Sun, X.; Li, X.; Ye, Y.; Tan, T.; Zhang, H.; Yang, C.; Han, J. W.; Chen, Y. Activating Lattice Oxygen in Perovskite Oxide by B-Site Cation Doping for Modulated Stability and Activity at Elevated Temperatures. *Adv. Sci.* **2021**, *8* (22), No. e2102713.
(10) Kim, B.-J.; Fabbri, E.; Abbott, D. F.; Cheng, X.; Clark, A. H.; Nachtegaal, M.; Borlaf, M.; Castelli, I. E.; Graule, T.; Schmidt, T. J. Functional Role of Fe-Doping in Co-Based Perovskite Oxide Catalysts for Oxygen Evolution Reaction. *J. Am. Chem. Soc.* **2019**, *141* (13), 5231−5240.
(11) Liu, Y.; Huang, H.; Xue, L.; Sun, J.; Wang, X.; Xiong, P.; Zhu, J. Recent advances in the heteroatom doping of perovskite oxides for efficient electrocatalytic reactions. *Nanoscale* **2021**, *13* (47), 19840−19856.
(12) Pradeep, K. R.; Elumalai, A.; Viswanatha, R. Effect of Electronic Structure on Delayed Fluorescence in Mn-Doped Perovskite Nanocrystals. *J. Phys. Chem. C* **2022**, *126* (23), 9813−9819.
(13) Koch, G.; Hävecker, M.; Teschner, D.; Carey, S. J.; Wang, Y.; Kube, P.; Hetaba, W.; Lunkenbein, T.; Auffermann, G.; Timpe, O.; Rosowski, F.; Schlögl, R.; Trunschke, A. Surface Conditions That Constrain Alkane Oxidation on Perovskites. *ACS Catal.* **2020**, *10* (13), 7007−7020.
(14) Büker, J.; Alkan, B.; Fu, Q.; Xia, W.; Schulwitz, J.; Waffel, D.; Falk, T.; Schulz, C.; Wiggers, H.; Muhler, M.; Peng, B. Selective cyclohexene oxidation with O 2, H 2 O 2 and tert -butyl hydroperoxide over spray-flame synthesized LaCo 1−x Fe x O 3 nanoparticles. *Catal. Sci. Technol.* **2020**, *10* (15), 5196−5206.
(15) He, X.; Dong, F.; Han, W.; Tang, Z.; Ding, Y. Recent advances and future challenges in the catalytic combustion of light hydrocarbon VOCs. *J. Mater. Chem. A* **2024**, *12* (13), 7470−7507.
(16) Tomás, R. A. F.; Bordado, J. C. M.; Gomes, J. F. P. p-Xylene oxidation to terephthalic acid: a literature review oriented toward process optimization and development. *Chem. Rev.* **2013**, *113* (10), 7421−7469.
(17) Pu, T.; Tian, H.; Ford, M. E.; Rangarajan, S.; Wachs, I. E. Overview of Selective Oxidation of Ethylene to Ethylene Oxide by Ag Catalysts. *ACS Catal.* **2019**, *9* (12), 10727−10750.
(18) Knoche, S.; Heid, M.; Gora, N.; Ohlig, D.; Drochner, A.; Etzold, B.; Vogel, H. Mechanistic Study on the Selective Oxidation of Acrolein to Acrylic Acid concerning the Role of Water. *ChemCatChem* **2020**, *12* (13), 3560−3575.
(19) Fu, C.; Du, J.; Shi, N.; Yang, L.; Che, Q.; Zhang, P. Strongly active and environmentally friendly WO3/C3N4 photocatalysts for converting cyclohexane to cyclohexanone under ambient conditions. *Sci. Rep.* **2024**, *14* (1), 17947.
(20) Kirar, J. S.; Gupta, N. M.; Chandra, K.; Vani, H. K.; Deswal, Y.; Khare, S. Selective oxidation of cyclohexane to KA oil over Co and Fe nanoparticles immobilized on layered double hydroxide nanocatalytic system. *New J. Chem.* **2024**, *48* (45), 19125−19135.
(21) Zheng, J.; Liu, J.; Feng, X.; Luo, Y.; Cai, W.; Liao, Z.; Fang, Y. One-step fabrication of Bi2MoO6 nanowires-g-C3N4 composites for outstanding photocatalytic performance in cyclohexane oxidation. *J. Alloys Compd.* **2025**, *1010*, 177367.
(22) Nowotny, M.; Pedersen, L. N.; Hanefeld, U.; Maschmeyer, T. Increasing the Ketone Selectivity of the Cobalt-Catalyzed Radical Chain Oxidation of Cyclohexane. *Chem. —Eur. J.* **2002**, *8* (16), 3724−3731.
(23) Schuchardt, U.; Cardoso, D.; Sercheli, R.; Pereira, R.; Da Cruz, R. S.; Guerreiro, M. C.; Mandelli, D.; Spinacé, E. V.; Pires, E. L. Cyclohexane oxidation continues to be a challenge. *Appl. Catal., A* **2001**, *211* (1), 1−17.
(24) Chavan, S. A.; Srinivas, D.; Ratnasamy, P. Oxidation of Cyclohexane, Cyclohexanone, and Cyclohexanol to Adipic Acid by a

Non-HNO3 Route over Co/Mn Cluster Complexes. *J. Catal.* **2002**, *212* (1), 39−45.
(25) Rodionova, L. I.; Smirnov, A. V.; Borisova, N. E.; Khrustalev, V. N.; Moiseeva, A. A.; Grünert, W. Binuclear cobalt complex with Schiff base ligand: Synthesis, characterization and catalytic properties in partial oxidation of cyclohexane. *Inorg. Chim. Acta* **2012**, *392*, 221−228.
(26) Pamin, K.; Tabor, E.; Górecka, S.; Kubiak, W. W.; Rutkowska-Zbik, D.; Połtowicz, J. Three Generations of Cobalt Porphyrins as Catalysts in the Oxidation of Cycloalkanes. *ChemSusChem* **2019**, *12* (3), 684−691.
(27) Tong, J.; Bo, L.; Cai, X.; Wang, H.; Zhang, Q.; Su, L. Aerobic Oxidation of Cyclohexane Effectively Catalyzed by Simply Synthesized Silica-Supported Cobalt Ferrite Magnetic Nanocrystal. *Ind. Eng. Chem. Res.* **2014**, *53* (25), 10294−10300.
(28) Xu, L.-X.; He, C.-H.; Zhu, M.-Q.; Fang, S. A highly active Au/Al2O3 catalyst for cyclohexane oxidation using molecular oxygen. *Catal. Lett.* **2007**, *114* (3−4), 202−205.
(29) Fu, S.; You, K.; Ni, W.; Chen, Z.; Zhao, F.; Yan, D.; Zhang, X.; Luo, H. One-step highly selective catalytic oxidation of cyclohexane to KA-oil over functional CeMn0.5Co0.5Ox composite oxide: Synergistic effects between Mn and Co species with different valences and metal ion ratios. *Chem. Eng. Sci.* **2023**, *277*, 118878.
(30) Sankar, G.; Raja, R.; Thomas, J. M. Redox solid catalysts for the selective oxidation of cyclohexane in air. *Catal. Lett.* **1998**, *55* (1), 15−23.
(31) Sreevardhan Reddy, S.; David Raju, B.; Padmasri, A. H.; Sai Prakash, P. K.; Rama Rao, K. S. Novel and efficient cobalt encapsulated SBA-15 catalysts for the selective oxidation of cyclohexane. *Catal. Today* **2009**, *141* (1−2), 61−65.
(32) Muhumuza, E.; Wu, P.; Nan, T.; Zhao, L.; Bai, P.; Mintova, S.; Yan, Z. Perovskite-Type LaCoO 3 as an Efficient and Green Catalyst for Sustainable Partial Oxidation of Cyclohexane. *Ind. Eng. Chem. Res.* **2020**, *59* (49), 21322−21332.
(33) Li, X.; Hao, S.; Chen, Z.; Huang, T.; Fu, S.; Zhao, F.; You, K.; Luo, H. Roles of the A-Site Ca Dopant in Modifying Surface Properties of a Co-Based Perovskite Catalyst for Selective Oxidation of Cyclohexane. *Ind. Eng. Chem. Res.* **2024**, *63* (14), 6087−6099.
(34) Büker, J.; Alkan, B.; Chabbra, S.; Kochetov, N.; Falk, T.; Schnegg, A.; Schulz, C.; Wiggers, H.; Muhler, M.; Peng, B. Liquid-Phase Cyclohexene Oxidation with O2 over Spray-Flame-Synthesized La1-x Srx CoO3 Perovskite Nanoparticles. *Chemistry* **2021**, *27* (68), 16912−16923.
(35) Geiss, J.; Büker, J.; Schulte, J.; Peng, B.; Muhler, M.; Winterer, M. LaCo 1− x Fe x O 3 Nanoparticles in Cyclohexene Oxidation. *J. Phys. Chem. C* **2023**, *127* (10), 5029−5038.
(36) Wang, Y.; Zhou, J.; Chen, Z.; Zhuge, X.; Wang, Z. Tailoring oxygen vacancies by synergy of dual metal cations in LaCo0.8M0.2O3 (M = Cu, Ni, Fe, Mn) towards catalytic oxidation of toluene. *J. Environ. Chem. Eng.* **2024**, *12* (5), 113555.
(37) Guo, N.; Wang, Z.; Yuan, C.; Wang, Z.; Jiang, L.; Wang, Q.; Du, Z.; Liu, Y. Insights into catalytic oxidation mechanism of toluene by lanthanum mangan-based perovskite in wet environment based on in-situ DRIFTS. *Sep. Purif. Technol.* **2025**, *353*, 128296.
(38) Kim, M.; Lee, H. Oxygen adsorption capability and electrochemical properties induced by oxygen vacancies in cerium-doped LaFeO3 perovskite oxide. *Scr. Mater.* **2024**, *242*, 115880.
(39) Jiang, Y.; Li, Z.; Zhu, T.; Li, D.; Wang, H.; Zhu, X. Oxygen Storage Characteristics and Redox Behaviors of Lanthanum Perovskite Oxides with Transition Metals in the B-Sites. *Energy Fuels* **2023**, *37* (13), 9419−9433.
(40) Ingavale, S.; Gopalakrishnan, M.; Enoch, C. M.; Pornrungroj, C.; Rittiruam, M.; Praserthdam, S.; Somwangthanaroj, A.; Nootong, K.; Pornprasertsuk, R.; Kheawhom, S. Strategic Design and Insights into Lanthanum and Strontium Perovskite Oxides for Oxygen Reduction and Oxygen Evolution Reactions. *Small* **2024**, *20* (19), No. e2308443.
(41) Hareendran, A.; Dreyer, M.; Sato, T.; Cosanne, N.; Leroy, C. L.; Peng, B.; Behrens, M.; Schnegg, A.; Muhler, M. Aerobic Oxidation of Cyclohexane over LaCoxFe1-xO3 Perovskites in the Liquid Phase. *Mol. Catal.* **2024**, *569*, 114615.
(42) Dreyer, M.; Cruz, D.; Hagemann, U.; Zeller, P.; Heidelmann, M.; Salamon, S.; Landers, J.; Rabe, A.; Ortega, K. F.; Najafishirtari, S.; Wende, H.; Hartmann, N.; Knop-Gericke, A.; Schlögl, R.; Behrens, M. The Effect of Water on the 2-Propanol Oxidation Activity of Co-Substituted LaFe1- Cox O3 Perovskites. *Chemistry* **2021**, *27* (68), 17127−17144.
(43) Dreyer, M.; Krebs, M.; Najafishirtari, S.; Rabe, A.; Friedel Ortega, K.; Behrens, M. The Effect of Co Incorporation on the CO Oxidation Activity of LaFe1−xCoxO3 Perovskites. *Catalysts* **2021**, *11* (5), 550.
(44) Shannon, R. D. Revised effective ionic radii and systematic studies of interatomic distances in halides and chalcogenides. *Acta Cryst. A* **1976**, *32* (5), 751−767.
(45) Mulcahy, M. F. R. The oxidation of hydrocarbons. Some observations on the induction period. *Trans. Faraday Soc.* **1949**, *45*, 575.
(46) Crombie, C. M.; Lewis, R. J.; Kovačič, D.; Morgan, D. J.; Davies, T. E.; Edwards, J. K.; Skjøth-Rasmussen, M. S.; Hutchings, G. J. The Influence of Reaction Conditions on the Oxidation of Cyclohexane via the In-Situ Production of H2O2. *Catal. Lett.* **2021**, *151* (1), 164−171.
(47) Schäfer, R.; Merten, C.; Eigenberger, G. Autocatalytic Cyclohexane Oxidation in a Bubble Column Reactor. *Can. J. Chem. Eng.* **2003**, *81* (3−4), 741−748.
(48) Srinivas, P.; Mukhopadhyay, M. Oxidation of Cyclohexane in Supercritical Carbon Dioxide Medium. *Ind. Eng. Chem. Res.* **1994**, *33* (12), 3118−3124.
(49) Suresh, A. K.; Sridhar, T.; Potter, O. E. Autocatalytic oxidation of cyclohexane—modeling reaction kinetics. *AIChE J.* **1988**, *34* (1), 69−80.
(50) Hermans, I.; Jacobs, P. A.; Peeters, J. To the core of autocatalysis in cyclohexane autoxidation. *Chem. —Eur. J.* **2006**, *12* (16), 4229−4240.
(51) Büker, J.; Huang, X.; Bitzer, J.; Kleist, W.; Muhler, M.; Peng, B. Synthesis of Cu Single Atoms Supported on Mesoporous Graphitic Carbon Nitride and Their Application in Liquid-Phase Aerobic Oxidation of Cyclohexene. *ACS Catal.* **2021**, *11* (13), 7863−7875.
(52) Tuo, B.; Wang, Z.; Ren, Z.; Zhang, H.; Lu, X.; Zhang, Y.; Zang, S.; Song, Y. A novel radical-reaction interruption strategy for enhancing the light stability of perovskite solar cells. *Energy Environ. Sci.* **2024**, *17* (8), 2945−2955.
(53) Li, L.; Hao, C.; Zhai, R.; He, W.; Deng, C. Study on the mechanism of free radical scavenger TEMPO blocking in coal oxidation chain reaction. *Fuel* **2023**, *331*, 125853.
(54) Fónagy, O.; Szabó-Bárdos, E.; Horváth, O. 1,4-Benzoquinone and 1,4-hydroquinone based determination of electron and superoxide radical formed in heterogeneous photocatalytic systems. *J. Photochem. Photobiol., A* **2021**, *407*, 113057.
(55) Martín-Gómez, J.; Pérez-Losada, M.; López-Tenllado, F. J.; Hidalgo-Carrillo, J.; Herrera-Beurnio, M. C.; Estévez, R.; Marinas, A.; Urbano, F. J. Insight into the reaction mechanism of photocatalytic production of solketal. *Catal. Today* **2024**, *429*, 114506.
(56) Tizaoui, C.; Grima, N. M.; Derdar, M. Z. Effect of the radical scavenger t-butanol on gas−liquid mass transfer. *Chem. Eng. Sci.* **2009**, *64* (21), 4375−4382.
(57) Garg, S.; Yuan, Y.; Mortazavi, M.; Waite, T. D. Caveats in the Use of Tertiary Butyl Alcohol as a Probe for Hydroxyl Radical Involvement in Conventional Ozonation and Catalytic Ozonation Processes. *ACS EST Eng.* **2022**, *2* (9), 1665−1676.
(58) Conte, M.; Liu, X.; Murphy, D. M.; Taylor, S. H.; Whiston, K.; Hutchings, G. J. Insights into the Reaction Mechanism of Cyclohexane Oxidation Catalysed by Molybdenum Blue Nanorings. *Catal. Lett.* **2016**, *146* (1), 126−135.
(59) Hermans, I.; Jacobs, P.; Peeters, J. The formation of byproducts in the autoxidation of cyclohexane. *Chem. —Eur. J.* **2007**, *13* (3), 754−761.

https://doi.org/10.1021/acscatal.5c02919
ACS Catal. 2025, 15, 12773−12789

(60) Biesinger, M. C.; Payne, B. P.; Grosvenor, A. P.; Lau, L. W.; Gerson, A. R.; Smart, R. S. Resolving surface chemical states in XPS analysis of first row transition metals, oxides and hydroxides: Cr, Mn, Fe, Co and Ni. *Appl. Surf. Sci.* **2011**, *257* (7), 2717−2730.
(61) Acosta Pérez, H.; López, C. A.; Furlong, O. J.; Nazzarro, M. S.; Marchetti, S. G.; Cadús, L. E.; Agüero, F. N. Highly Resistant LaCo1−xFexO3 Perovskites Used in Chlorobenzene Catalytic Combustion. *Catalysts* **2023**, *13* (1), 42.
(62) Al-Mamari, R. T.; Widatallah, H. M.; Elzain, M. E.; Gismelseed, A. M.; Al-Rawas, A. D.; Al-Harthi, S. H.; Myint, M. T. Z.; Al-Saqri, N.; Al-Abri, M. Author Correction: Core and surface structure and magnetic properties of mechano-synthesized LaFeO3 nanoparticles and their Eu3+ -doped and Eu3+/Cr3+ -co-doped variants. *Sci. Rep.* **2024**, *14* (1), 21307.
(63) Sharma, N.; Kushwaha, H. S.; Sharma, S. K.; Sachdev, K. Fabrication of LaFeO3 and rGO-LaFeO3 microspheres based gas sensors for detection of NO2 and CO. *RSC Adv.* **2020**, *10* (3), 1297−1308.
(64) Dupin, J.-C.; Gonbeau, D.; Vinatier, P.; Levasseur, A. Systematic XPS studies of metal oxides, hydroxides and peroxides. *Phys. Chem. Chem. Phys.* **2000**, *2* (6), 1319−1324.
(65) Zi, Z.; Sun, Y.; Zhu, X.; Yang, Z.; Dai, J.; Song, W. Synthesis and magnetic properties of CoFe2O4 ferrite nanoparticles. *J. Magn. Magn. Mater.* **2009**, *321* (9), 1251−1255.
(66) Eskandari, N.; Nabiyouni, G.; Masoumi, S.; Ghanbari, D. Preparation of a new magnetic and photo-catalyst CoFe2O4−SrTiO3 perovskite nanocomposite for photo-degradation of toxic dyes under short time visible irradiation. *Composites, Part B* **2019**, *176*, 107343.
(67) Berry, F. J.; Gancedo, J.; Marco, J. F.; Ren, X. Synthesis and characterization of the reduction properties of cobalt-substituted lanthanum orthoferrites. *J. Solid State Chem.* **2004**, *177* (6), 2101−2114.
(68) Sayler, R. I.; Hunter, B. M.; Fu, W.; Gray, H. B.; Britt, R. D. EPR Spectroscopy of Iron- and Nickel-Doped [ZnAl]-Layered Double Hydroxides: Modeling Active Sites in Heterogeneous Water Oxidation Catalysts. *J. Am. Chem. Soc.* **2020**, *142* (4), 1838−1845.
(69) Hansen, H. C. B.; Koch, C. B.; Taylor, R. M. Synthesis and Characterization of Cobalt(II)-Iron(III) Hydroxide Carbonate, a Layered Double Hydroxide Belonging to the Pyroaurite Group. *J. Solid State Chem.* **1994**, *113* (1), 46−53.
(70) Hadi, J.; Grangeon, S.; Warmont, F.; Seron, A.; Greneche, J.-M. A novel and easy chemical-clock synthesis of nanocrystalline iron-cobalt bearing layered double hydroxides. *J. Colloid Interface Sci.* **2014**, *434*, 130−140.
(71) Shankar Naik, S.; Theerthagiri, J.; Nogueira, F. S.; Lee, S. J.; Min, A.; Kim, G.-A.; Maia, G.; Pinto, L. M.; Choi, M. Y. Dual-Cation-Coordinated CoFe-Layered Double-Hydroxide Nanosheets Using the Pulsed Laser Ablation Technique for Efficient Electrochemical Water Splitting: Mechanistic Screening by In Situ/Operando Raman and Density Functional Theory Calculations. *ACS Catal.* **2023**, *13* (2), 1477−1491.
(72) Yang, X.; Cheng, J.; Xu, Y.; Li, H.; Tu, W.; Zhou, J. Heterogeneous ultra-thin FeCo-LDH@Co(OH)2 nanosheets facilitated electrons transfer for oxygen evolution reaction. *Chem. Eng. J.* **2023**, *472*, 145076.
(73) Gnezdilov, V.; Fomin, V.; Yeremenko, A. V.; Choi, K.-Y.; Pashkevich, Y.; Lemmens, P.; Shiryaev, S.; Bychkov, G.; Barilo, S. Low-temperature mixed spin state of Co3+ in LaCoO3 evidenced from Jahn−Teller lattice distortions. *Low-Temp. Phys.* **2006**, *32* (2), 162−168.
(74) Bhowmick, T.; Nag, S.; Majumder, S. B. Investigations on lanthanum iron cobalt oxide thin film as selective carbon monoxide sensor. *J. Alloys Compd.* **2021**, *884*, 161161.
(75) Thirumalairajan, S.; Girija, K.; Hebalkar, N. Y.; Mangalaraj, D.; Viswanathan, C.; Ponpandian, N. Shape evolution of perovskite LaFeO3 nanostructures: a systematic investigation of growth mechanism, properties and morphology dependent photocatalytic activities. *RSC Adv.* **2013**, *3* (20), 7549.
(76) Eyméoud, P.; Turquat, C.; Pardanaud, C.; Leroux, C.; Merlen, A. Raman spectroscopic detection of vacancies in LaFeO3. *Mater. Lett.* **2023**, *330*, 133296.
(77) Li, Y.; Qiu, W.; Qin, F.; Fang, H.; Hadjiev, V. G.; Litvinov, D.; Bao, J. Identification of Cobalt Oxides with Raman Scattering and Fourier Transform Infrared Spectroscopy. *J. Phys. Chem. C* **2016**, *120* (8), 4511−4516.
(78) Rivas-Murias, B.; Salgueiriño, V. Thermodynamic CoO−Co 3 O 4 crossover using Raman spectroscopy in magnetic octahedron-shaped nanocrystals. *J. Raman Spectrosc.* **2017**, *48* (6), 837−841.
(79) Ravindra, A. V.; Behera, B. C.; Padhan, P.; Lebedev, O. I.; Prellier, W. Tailoring of crystal phase and Néel temperature of cobalt monoxides nanocrystals with synthetic approach conditions. *J. Appl. Phys.* **2014**, *116* (3), 033912.
(80) Bai, F.; Schulwitz, J.; Priamushko, T.; Hagemann, U.; Kostka, A.; Heidelmann, M.; Cherevko, S.; Muhler, M.; Li, T. Correlating atomic-scale structural and compositional details of Ca-doped LaCoO3 perovskite nanoparticles with activity and stability towards the oxygen evolution reaction. *J. Catal.* **2024**, *438*, 115697.
(81) Behera, S.; Kamble, V. B.; Vitta, S.; Umarji, A. M.; Shivakumara, C. Synthesis, structure and thermoelectric properties of $La_{1-x}Na_xCoO_3$ perovskite oxides. *Bull. Mater. Sci.* **2017**, *40* (7), 1291−1299.
(82) Bhattacharyya, K.; Auer, A. A. Oxygen Evolution Reaction Electrocatalysis on Cobalt(oxy)hydroxide: Role of Fe Impurities. *J. Phys. Chem. C* **2022**, *126* (44), 18623−18635.
(83) Bajdich, M.; García-Mota, M.; Vojvodic, A.; Nørskov, J. K.; Bell, A. T. Theoretical investigation of the activity of cobalt oxides for the electrochemical oxidation of water. *J. Am. Chem. Soc.* **2013**, *135* (36), 13521−13530.
(84) Mavros, M. G.; Tsuchimochi, T.; Kowalczyk, T.; McIsaac, A.; Wang, L.-P.; van Voorhis, T. What can density functional theory tell us about artificial catalytic water splitting? *Inorg. Chem.* **2014**, *53* (13), 6386−6397.
(85) Turrà, N.; Neuenschwander, U.; Baiker, A.; Peeters, J.; Hermans, I. Mechanism of the catalytic deperoxidation of tert-butylhydroperoxide with cobalt(II) acetylacetonate. *Chemistry* **2010**, *16* (44), 13226−13235.
(86) Abbasi, M.; Slavinskaya, N.; Riedel, U. Low Temperature Oxidation of Cyclohexane: Uncertainty of Important Thermo-Chemical Properties. *Eurasian Chem. Technol. J.* **2018**, *4*, 263−275.

https://doi.org/10.1021/acscatal.5c02919
ACS Catal. 2025, 15, 12773−12789